

We are IntechOpen, the world's leading publisher of Open Access books Built by scientists, for scientists

6,900

Open access books available

186,000

International authors and editors

200M

Downloads

Our authors are among the

154

Countries delivered to

TOP 1%

most cited scientists

12.2%

Contributors from top 500 universities



WEB OF SCIENCE™

Selection of our books indexed in the Book Citation Index
in Web of Science™ Core Collection (BKCI)

Interested in publishing with us?
Contact book.department@intechopen.com

Numbers displayed above are based on latest data collected.
For more information visit www.intechopen.com



Manipulating the Electromagnetic Wave with a Magnetic Field

Shiyang Liu¹, Zhifang Lin² and S. T. Chui³

¹*Institute of Information Optics, Zhejiang Normal University*

²*Surface Physics Laboratory, Department of Physics, Fudan University*

³*Department of Physics and Astronomy, University of Delaware*

^{1,2}China

³USA

1. Introduction

Metamaterials are composite, artificial materials, composed of sub-wavelength building blocks acting like man-made atoms, which exhibit novel and unique electromagnetic (EM) properties, not occurring in natural materials (Pendry, 2000; Shelby et al., 2001). With the advent of metamaterials the molding of the flow of light becomes more and more flexible. Exhilaratingly, through the state-of-art design of metamaterial, nearly arbitrary profile of EM constitutive parameters can be engineered, enabling the manifestation of an unprecedented variety of exotic behaviors from microwave region to optical region such as negative refraction (Shalaev, 2007; Valentine et al., 2008), cloaking (Leonhardt, 2006; Pendry et al, 2006; Schurig et al., 2006), and subwavelength propagation (Maier, 2002; Maier et al., 2003) of EM wave. Metamaterials are attracting more and more theorist, experimentalist, and engineers from many research fields. With the further development, we can expect a revolutionary influence that metamaterials will offer in the field of microwave engineering, opto-electronic information technology, even photonics and optical communication.

The building blocks are usually made of metallic material (Pendry et al., 1996; 1999), accompanied with the drawbacks of intrinsic loss and tunability limitation. Here we present a class of metamaterials composed of building blocks made of magnetic material, which are accordingly called magnetic metamaterials (MM). Due to the dependence of permeability on external magnetic field (EMF), the EM properties of MM can be manipulated by an EMF, providing us with more degrees of tunability. For this reason, MM can be a promising candidate for the design of optical devices. In addition, different from dielectric or metallic materials, the permeability of magnetic material is a second rank tensor with nonzero off-diagonal elements. The time reversal symmetry is thus broken in MM systems (Wang et al., 2008), based on which we can observe some other phenomena and design special optical devices. Besides, we also examine the EM properties of a kind of magnetic photonic crystal (MPC) and magnetic graded PC (MGPC), made of an array of ferrite rods periodically arranged in air under uniform and nonuniform EMFs. They can also offer us the manipulability on the flow of EM wave with the tunability by an EMF.

The research content of the present chapter consists of four parts. In the first part, we examine the mechanism governing the photonic band gaps (PBGs) of a two dimensional (2D) MPC,

based on the simulations on the photonic band diagrams and the transmission spectra, by which we can identify three different types of PBGs. In particular, it is shown that “magnetic surface plasmon” (MSP) resonance induced PBGs can be completely tunable by an EMF and robust against position and size disorder of the ferrite rods. In the second part, we develop an effective-medium theory (EMT) within the coherent potential approximation, which is specially suitable to retrieve the effective constitutive parameters of the anisotropic MM. In addition, we demonstrate a construction of negative index metamaterial (NIM) based on MM, which possesses effective constitutive parameters $\epsilon_{\text{eff}} = \mu_{\text{eff}} = -1$ and the magnetically tunable working frequency. In the third part, we propose and conceptualize an alternative type of graded PC, MGPC. With the MGPC, we can also mold the flow of EM wave, resulting in the focusing effect and the mirage effect for an TM Gaussian beam. In fourth part, we examine the reflection behavior of an EM waves from an MM slab. It is demonstrated that at some frequency the reflected wave is found to exhibit a giant circulation in that locally the angular momenta of the components are all of the same sign due to the MSP resonance and the broken of time reversal symmetry (TRS). As a result of this finite circulation, a dramatic change is exhibited for beams incident from different directions.

2. Formation of the robust and magnetically tunable photonic band gap

PCs or PBG materials have attracted more and more attentions since the conception was brought out in the 1980s (John, 1987; Yablonovitch, 1987) and became the subject of intensive theoretical and experimental research due to their promising applications in micro- and optoelectronics (Joannopoulos et al., 1995). One unique characteristic of PCs is the existence of PBGs, the frequency ranges over which all EM modes are forbidden, which offers much more flexibilities in manipulating the EM waves. To make it more applicable, tunable PCs have been proposed and investigated, where the PBGs can be modulated extrinsically by some external parameters such as the electric field (Busch & John, 1999; Kang et al., 2001), the magnetic field (Figotin et al., 1998; Golosovsky et al., 1999; Kee et al., 2000), the temperature (Halevi & Ramos-Mendieta, 2000; Kee & Lim, 2001), or the strain (Kim & Gopalan, 2001). Here, we shall concentrate on the effect of EMF on the PBGs of MPCs. As a typical tunable PC, MPCs have attracted a lot of interest (Chen et al., 2007; Inoue et al., 2006; Lin & Chui, 2007; Liu et al., 2008; Lyubchanskii et al., 2003; Sigalas et al., 1997) due to the fast switching time of magnetic systems and the potential tunability of the PBGs by the EMF.

2.1 Band structure calculations of the PBG materials

To illustrate the typical behavior of the photonic band diagram of an MPC, we consider the example of a 2D hexagonal lattice of ferrite rods in the nonmagnetic plexiglas background, with the lattice constant a and rod axes along z direction. When fully magnetized, the magnetic permeability in form (Pozar, 2004)

$$\hat{\mu} = \begin{pmatrix} \mu_r & -i\mu_\kappa & 0 \\ i\mu_\kappa & \mu_r & 0 \\ 0 & 0 & 1 \end{pmatrix}, \quad \hat{\mu}^{-1} = \begin{pmatrix} \mu'_r & -i\mu'_\kappa & 0 \\ i\mu'_\kappa & \mu'_r & 0 \\ 0 & 0 & 1 \end{pmatrix}, \quad (1)$$

with

$$\mu_r = 1 + \frac{\omega_m(\omega_0 - i\alpha\omega)}{(\omega_0 - i\alpha\omega)^2 - \omega^2}, \quad \mu_\kappa = \frac{\omega_m\omega}{(\omega_0 - i\alpha\omega)^2 - \omega^2}, \quad \mu'_r = \frac{\mu_r}{\mu_r^2 - \mu_\kappa^2}, \quad \mu'_\kappa = \frac{-\mu_\kappa}{\mu_r^2 - \mu_\kappa^2},$$

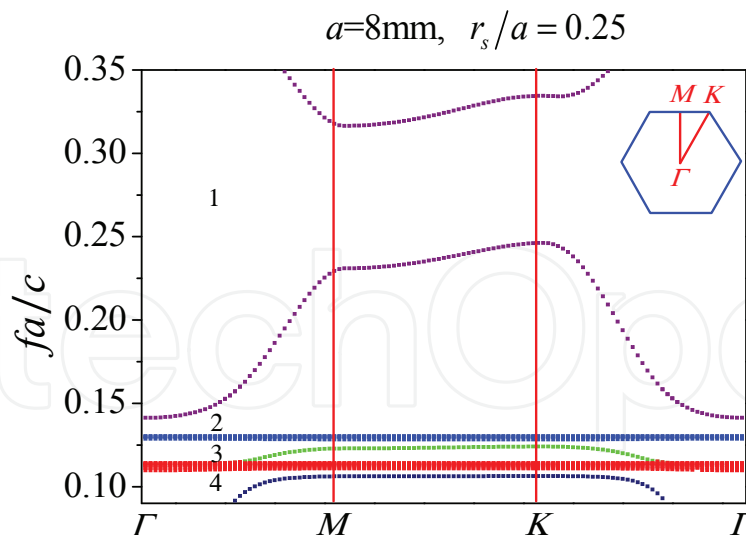


Fig. 1. The photonic band diagram of a 2D hexagonal MPC, with $a = 8$ mm, $r = 2$ mm, and $H_0 = 900$ Oe. The reduced Brillouin zone is shown in the inset together with the high symmetry points. Four PBGs marked with 1, 2, 3, and 4, exist from high to low frequency.

where $\omega_0 = \gamma H_0$ is the resonance frequency with $\gamma = 2.8$ MHz/Oe the gyromagnetic ratio; H_0 the sum of the EMF applied in z direction and the shape anisotropy field Pozar (2004), $\omega_m = 4\pi\gamma M_s$ is the characteristic frequency with $4\pi M_s$ the saturation magnetization, and α is the damping coefficient of the ferrite. In the calculation of photonic band diagram, we set $\alpha = 0$ (Wang et al., 2008) and consider the transverse magnetic (TM) mode only.

Most photonic band diagram calculations have been based on the plane-wave expansion method (Ho et al., 1990) or the finite difference time domain method (Chan et al., 1995). However, for dispersive systems with gyromagnetic scatterer, it is rather difficult to achieve a reliable convergence of the solutions. In our work, the multiple scattering method (MSM) is employed, which is proved to be most powerful for the PCs consisting of non-overlap spheres or circular cylinders (Li & Zhang, 1998; Lin & Chui, 2004; 2007; Liu & Lin, 2006; Moroz, 2002; Stefanou et al., 1998).

We have shown a typical photonic band diagram in Fig. 1 for $H_0 = 900$ Oe, where the lattice constant is $a = 8$ mm, and the radius of the ferrite rod is $r_s = \frac{1}{4}a = 2$ mm. The relative permittivity and permeability of the nonmagnetic plexiglas are $\epsilon_m = 2.6$ and $\mu_m = 1$. For the ferrite rod $\epsilon_s = 12.3$ and the saturation magnetization $4\pi M_s = 1700$ gauss. The reduced Brillouin zone is illustrated as well in the inset. The corresponding high symmetry points are $\Gamma = \frac{2\pi}{a}(0,0)$, $M = \frac{2\pi}{a}(0, \frac{1}{\sqrt{3}})$, and $K = \frac{2\pi}{a}(\frac{1}{3}, \frac{1}{\sqrt{3}})$ with c the speed of light in vacuum. It can be seen that there exist four PBGs centered at $fa/c = 0.275, 0.138, 0.130,$ and 0.108 , labeled by 1, 2, 3, and 4, respectively, in Fig. 1. Later on, we will examine the origin and the tunability of these PBGs by an EMF.

Firstly, let us focus on the 1st PBG centered at $fa/c = 0.275$. To understand the origin of this PBG, we present in Fig. 2 the amplified part of the band diagram around this PBG, together with the band diagram for a scaled system with $a = 5$ mm. It can be found that both PBGs are centered at almost the same position in reduced frequency of c/a . In addition, the photonic band diagram around the PBG are also similar, showing a pretty good scale-length invariant behavior. It is the characteristic of the PBG originating from the Bragg scattering. To illustrate the effect of an EMF on this PBG, we also present the band diagram in Fig. 3 for $H_0 = 700$ Oe (a) and $H_0 = 900$ Oe (b), while keeping all the other parameters the same as in Fig. 1. It can

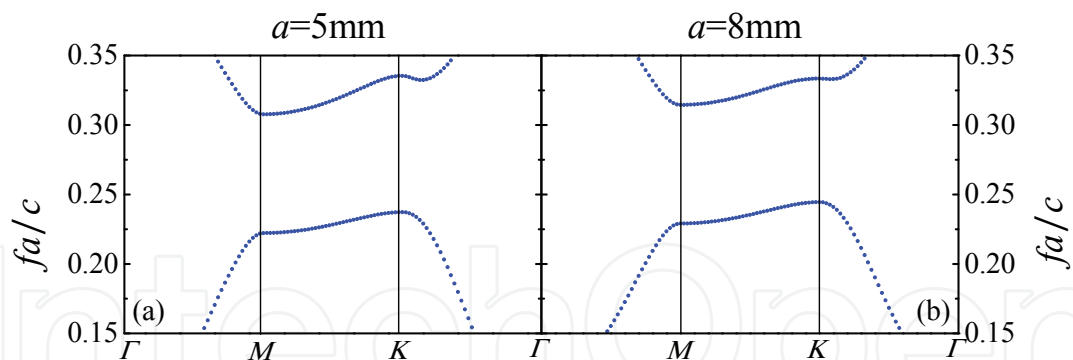


Fig. 2. The photonic band diagram near the 1st PBG of a 2D MPC with $a = 5$ mm (a) and $a = 8$ mm (b), while keeping all the other parameters the same as those in Fig. 1.

be found that the two band diagrams are nearly the same, suggesting that the EMF has a very weak effect on the 1st PBG. This explains the recent experimental results that show a tiny shift of the PBGs in response to the change of the EMF (Chen et al., 2007).

Next, let us examine the 2nd PBG centered at $fc/a = 0.138$. To demonstrate the effect of the EMF, we have calculated the photonic band diagram near the 2nd PBG as shown in Fig. 4(a) where $H_0 = 700$ Oe and all the other parameters are the same as those in Fig. 1. For comparison, we have also shown in Fig. 4(b) the corresponding part of Fig. 1. Different from the 1st PBG, a significant change can be observed in Fig. 4. The increase of the EMF shifts the 2nd PBG upwards substantially, so do the 3rd and 4th PBGs, suggesting that the 2nd PBG are intimately dependent on the magnetic permeability of the ferrite rod. An important characteristic is the appearance of a dense sets of flat bands between the 2nd and the 3rd PBGs in Fig. 4, signifying the occurrence of some kind of resonance.

In the study of plasmonics (Zayats et al., 2005), flat photonic bands have been observed near the surface plasmon frequency (McGurn & Maradudin, 1993; Kuzmiak et al., 1994) with $\epsilon = -1$ in 2D. In our case the flat bands occur when the effective magnetic susceptibility $\mu_r + \mu_k = -1$ at frequency $f_s = \frac{1}{2\pi} \left(\omega_0 + \frac{1}{2}\omega_m \right)$, which can be considered as the magnetic analog of the surface plasmon in metal. For the MPC under investigation, with $4\pi M_s = 1700$ gauss and $a = 8$ mm, we have $f_s a/c = 0.1158$ and 0.1308 for $H_0 = 700$ Oe and $H_0 = 900$ Oe, respectively. It can be seen clearly from Fig. 4 that f_s is near the top of the flat bands, above and below which open up the 2nd and 3rd PBGs, respectively. As a result, the 2nd and 3rd PBGs are governed by the resonance at frequency f_s . We have also studied the photonic band diagram

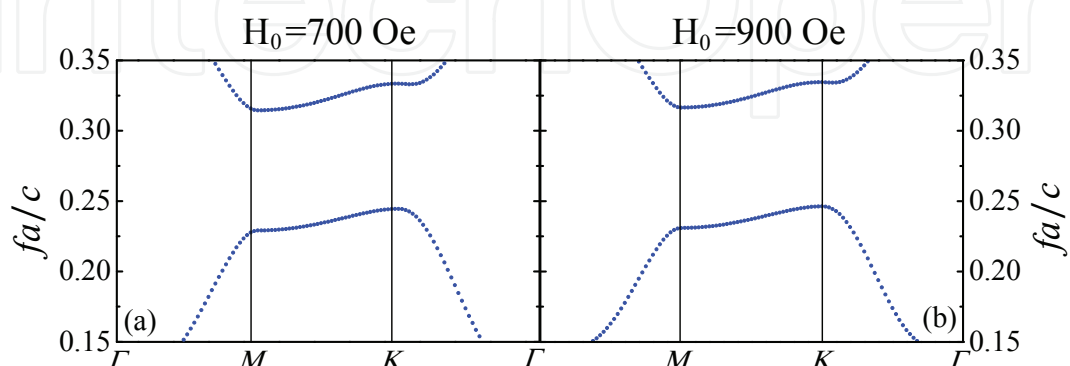


Fig. 3. (a) The photonic band diagram near the 1st PBG of a 2D MPC with $H_0 = 700$ Oe and all the other parameters the same as those in Fig. 1. (b) The same as that in Fig. 2(b).

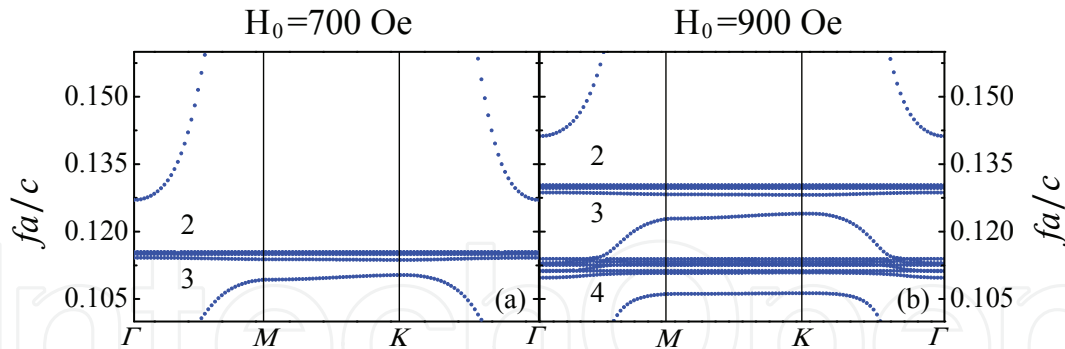


Fig. 4. (a) The photonic band diagram near the 2nd and 3rd PBGs of a 2D hexagonal MPC with $H_0 = 700$ Oe and all the other parameters the same as those in Fig. 1. (b) The same as that in Fig. 2(b). Numbers in the figure label the indices of the PBGs as shown in Fig. 1.

for systems with the lattice constants scaled by a variety of factors. Typical results are shown in Fig. 5, where we fixed $H_0 = 700$ Oe and scaled system from $a = 5$ mm to $a = 8$ mm. It can be found that the flat bands between the 2nd and the 3rd PBGs are located at the same frequency, indicating the independence of the flat bands on the lattice constant and rules out the possibility of the Bragg scattering mechanism. The flat bands is solely determined by f_s and therefore depends on the EMF and the saturation magnetization only.

In the end, we examine the 4th PBG in Fig. 1, above which there also appears a dense set of flat bands, implying once again some kind of resonance. From Eq. (1), it can be found that $\mu_r = \mu'_r = 0$ at a frequency $f_m = \frac{1}{2\pi} \sqrt{\omega_0(\omega_0 + \omega_m)}$. Accordingly, the wave vector inside the ferrite cylinder (proportional to $1/\sqrt{\mu'_r}$) tends to infinity at frequency f_m , corresponding to the occurrence of the “spin wave resonance”. For our system with $H_0 = 900$ Oe, we have $f_m = 0.114c/a$, corresponding to the top of the flat bands, as shown in Fig. 4(b). The frequency of the 4th PBG can therefore be tuned by the EMF in a similar way as the case for the 2nd and 3rd PBGs.

2.2 Simulations on the transmission coefficients

To examine the PBGs further, we have also performed simulations on the transmission coefficients, which can be expressed as the forward scattering amplitude of the MPC (Li & Zhang, 1998). Different from the calculation of photonic bands, in this section we adopt the practical material parameters and take into account the absorption of the sample.

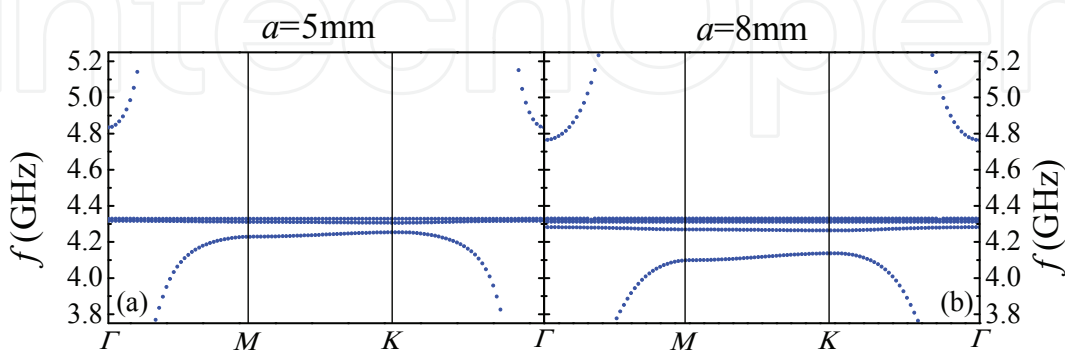


Fig. 5. The photonic band diagram near the 2nd and 3rd PBGs of a 2D hexagonal MPC with $a = 5$ mm (a) and $a = 8$ mm (b), respectively. The applied EMF is such that $H_0 = 700$ Oe, while all the other parameters are the same as those in Fig. 1.

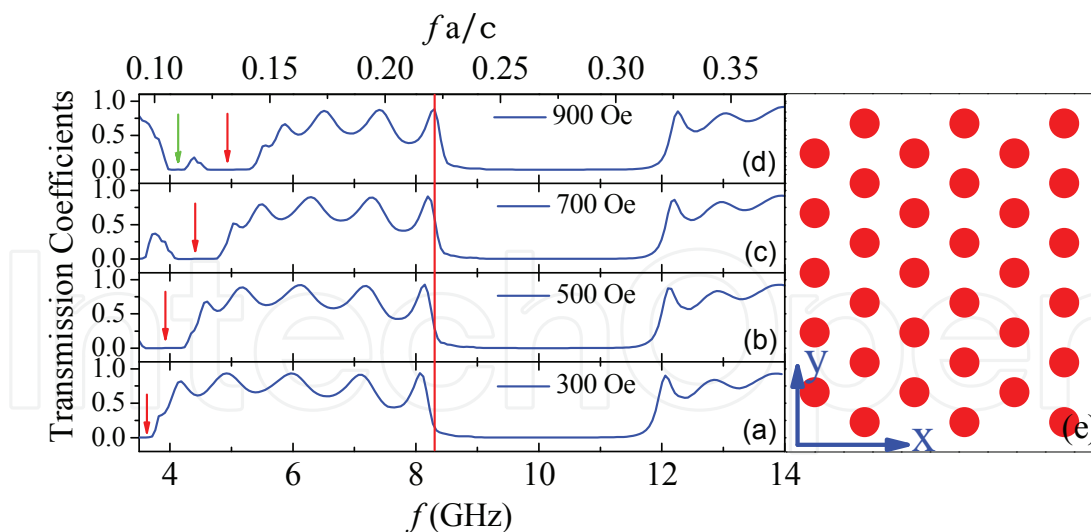


Fig. 6. Transmission coefficients of a 7-layer MPC slab under EMF $H_0 = 300$ Oe (a), 500 Oe (b), 700 Oe (c), and 900 Oe (d). The lattice constant is $a = 8$ mm and the radius of the ferrite rod is $r_s = \frac{1}{4}a = 2$ mm. The right panel (e) is the sample configuration.

Concretely, $\varepsilon_b = 2.6 + i5 \times 10^{-3}$, $\varepsilon_s = 12.3 + i6 \times 10^{-4}$, $\mu_b = 1.0$, and μ is given by Eq. (1) with damping coefficient taken as $\alpha = 7 \times 10^{-3}$ (Chen et al., 2007; Pozar, 2004).

Typical results for different H_0 are shown in Fig. 6 where the sample is a 7-layer slab with $a = 8$ mm and $r_s = \frac{1}{4}a$, as schematically illustrated in Fig. 6(e). It can be seen from Fig. 6 that with the increase of the EMF the 2nd, the 3rd (denoted by the red arrows), and the 4th PBGs (denoted by the green arrow) shift significantly to higher frequencies. However, the 1st PBG shows only a tiny shift when H_0 is varied from 300 Oe to 900 Oe. The transmission coefficients are in quantitative agreement with the photonic band diagram calculations. To be specific, the middle frequency of the 1st transmission gap in Fig. 6(d) is about $0.275c/a$; the middle frequency of the 2nd transmission gap (denoted by the red arrows) is located around $0.135c/a$; the 3rd transmission gap (denoted by the green arrow) has the middle frequency $0.125c/a$. They correspond exactly to the corresponding part of the photonic band diagram. From the analysis of the photonic band diagrams, we know that the 2nd, the 3rd, and the 4th PBGs arise from the resonance of the individual ferrite rod. Therefore, we can expect that the

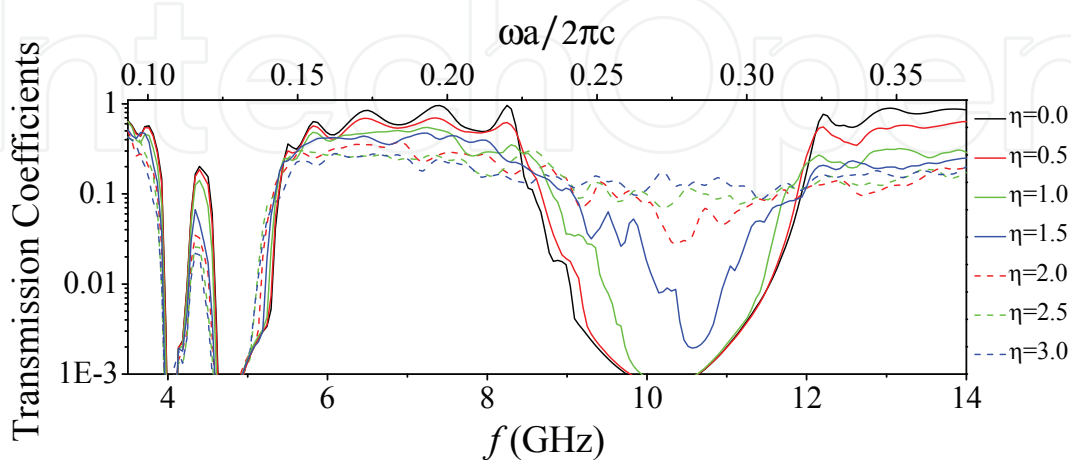


Fig. 7. Transmission coefficients of a 7-layer MPC slab under EMF $H_0 = 900$ Oe and with the position disorder characterized by η . Lattice constant $a = 8$ mm and radius $r_s = 2$ mm.

PBGs are robust against the position disorder. This is corroborated by the simulation on the transmission, where the disorder is introduced so that the position of each rod is displaced by $d_i = \zeta \cdot \eta \cdot d_{i0}$ with $i = x$ or y . Here, ζ is a random number uniformly distributed between -0.5 and 0.5 , $d_{x0} = \frac{\sqrt{3}}{2}a - 2r$ and $d_{y0} = a - 2r$ are the maximum position variations along x and y directions, η is a parameter introduced to measure the degree of disorder. In Fig. 7, we present the transmission coefficients with different randomness η . The corresponding parameters are the same as in Fig. 5 except that H_0 is fixed at 900 Oe. The results are obtained by averaging 20 realizations of the disordered system. It can be seen that with the increase of disorder the 1st PBG becomes narrower and narrower and disappears eventually due to the breakdown of the Bragg scattering. However, the resonance-induced PBGs remain essentially unchanged. Accordingly, it can be concluded that the introduction of the positional disorder affects only the Bragg type of PBG significantly, while the other two types of PBGs arising from resonance are quite robust against the position disorder. The similar effect has also been demonstrated in the systems consisting of electric active entities (Modinos et al., 2000; Yannopapas & Vitanov, 2006).

3. Negative index material manipulable with an external magnetic field

A particularly important class of metamaterials is the NIM (Pendry, 2000). Its corresponding properties were theoretically proposed by Veselago as early as in 1968 (Veselago, 1968). However, it is only fairly recently that the NIMs were experimentally realized based on Pendry's scheme, and then the interest in such material surged immediately. Various schemes are proposed and proved to possess the negative refractive index (Dolling et al., 2006; Liu et al., 2008; Peng et al., 2007; Rachford et al., 2007; Zhang et al., 2005; 2009). To investigate and characterize the optical properties of the metamaterials, it is crucial to retrieve the effective constitutive parameters (Chen et al., 2004; Jin et al., 2009; Koschny et al., 2003; 2005; Sarychev et al., 2000; Smith et al., 2002; 2005; Wu et al., 2006). In this section, we will present the EMT developed specially for the anisotropic MM. In particular, a ferrite-based NIM with $\mu_{\text{eff}} = \varepsilon_{\text{eff}} = -1$ is designed, which exhibits the negative refraction and the superlens effect.

3.1 Effective-medium theory for anisotropic magnetic metamaterials

We present in this section the formulation of the EMT for anisotropic MM in the 2D case, generalization to three dimensions is straightforward. For convenience, we consider a system made of ferrite rods with permittivity ε_s and magnetic permeability $\hat{\mu}$ given in Eq. (1) arranged periodically as a square lattice in an isotropic homogeneous medium with permittivity ε_0 and permeability μ_0 . The geometry of the system is shown in Fig. 8 where the rod axes are along z direction and the radii of the ferrite rods are r_s . We consider the TM mode with an anisotropic and tunable permeability.

The scheme of the EMT is as follows: (i) Transform the discrete periodic system in figure 8(a) into the effective medium with effective constitutive parameters ε_{eff} and μ_{eff} in figure 8(b); (ii) Take the unit cell of the MM as an equal-area coated rod with ferrite rod as its inner core and the background medium as the coated layer with radius $r_0 = a/\sqrt{\pi}$; (iii) The effective constitutive parameters ε_{eff} and μ_{eff} are determined by the condition that the scattering cross section of the coated rod in the effective medium vanishes in the long wave limit $k_{\text{eff}}r_0 \ll 1$ where $k_{\text{eff}} = k_0\sqrt{\varepsilon_{\text{eff}}\mu_{\text{eff}}}$ with k_0 the wave-number in the vacuum, $\mu_{\text{eff}} = (\mu_{re}^2 - \mu_{ke})^2 / \mu_{re} \cdot \mu_{re}$ and μ_{ke} are the components of the effective magnetic permeability tensor. The concept of our theory is the so-called coherent potential approximation (CPA) (Sheng et al., 1995), which has

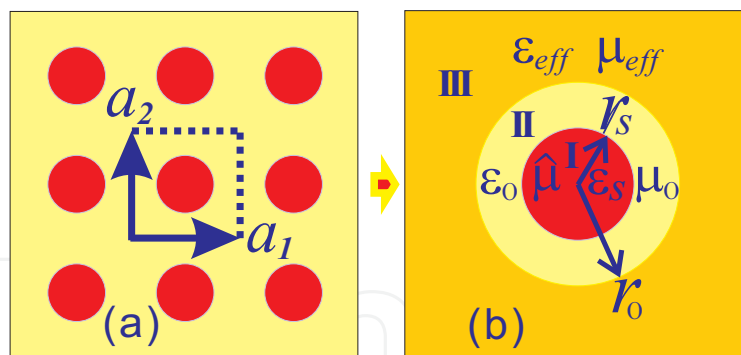


Fig. 8. (a) A 2D anisotropic MM consisting of the ferrite rods arranged as square lattice in the air background, and (b) its corresponding geometry in the effective-medium theory. The red circles, light yellow region, and dark yellow region correspond to the ferrite rods, the isotropic homogeneous background, and effective medium, respectively.

been used to retrieve the effective isotropic parameters for the EM (Hu et al., 2006; Wu et al., 2006), acoustic (Hu et al., 2008), and even elastic metamaterials (Wu et al., 2007).

As the procedure of the Mie theory, we expand the EM waves in regions I, II, and III of figure 8(b) into the summation of the vector cylindrical wave functions (VCWFs)

$$\mathbf{L}_n^{(J)}(k, \mathbf{r}) = \left[\frac{dz_n^{(J)}(\rho)}{d\rho} \mathbf{e}_r + \frac{in}{\rho} z_n^{(J)}(\rho) \mathbf{e}_\phi \right] e^{in\phi}, \quad (2a)$$

$$\mathbf{M}_n^{(J)}(k, \mathbf{r}) = \left[\frac{in}{\rho} z_n^{(J)}(\rho) \mathbf{e}_r - \frac{dz_n^{(J)}(\rho)}{d\rho} \mathbf{e}_\phi \right] e^{in\phi}, \quad (2b)$$

$$\mathbf{N}_n^{(J)}(k, \mathbf{r}) = z_n^{(J)}(\rho) e^{in\phi} \mathbf{e}_z, \quad (2c)$$

with k the wave vector, $\mathbf{r} = r \cos \phi \mathbf{e}_x + r \sin \phi \mathbf{e}_y$ the position vector, $\rho = kr$, $z_n^{(J)}(\rho)$ the Bessel function $J_n(\rho)$ and the first kind Hankel function $H_n^{(1)}(\rho)$ for $J = 1$ and 3 , respectively. For the EM field in the region I

$$\mathbf{E}_s(k_s, \mathbf{r}) = \sum_n q_n^s \mathbf{N}_n^{s(1)}, \quad \mathbf{H}_s(k_s, \mathbf{r}) = \sum_n \frac{k_s}{i\omega} q_n^s \left[i\mu'_{ks} \mathbf{L}_n^{s(1)} + \mu'_{rs} \mathbf{M}_n^{s(1)} \right], \quad (3)$$

where $k_s = k_0 \sqrt{\epsilon_s} \sqrt{\mu_s}$ with $\mu_s = (\mu_{rs}^2 - \mu_{ks}^2) / \mu_{rs} = 1 / \mu'_{rs}$, μ_{rs} , and μ_{ks} are given in equation (1), the superscript s in q_n^s means k_s is involved in VCWFs. In the coated layer area, *i.e.*, in region II the corresponding EM field components are

$$\mathbf{E}_b(k_0, \mathbf{r}) = \sum_n \left[q_n^0 \mathbf{N}_n^{0(1)} - b_n^0 \mathbf{N}_n^{0(3)} \right], \quad \mathbf{H}_b(k_0, \mathbf{r}) = \sum_n \frac{k_0}{i\omega \mu_0} \left[q_n^0 \mathbf{M}_n^{0(1)} - b_n^0 \mathbf{M}_n^{0(3)} \right], \quad (4)$$

where the superscript 0 in q_n^0 means k_0 is involved in VCWFs. Finally, in region III, we have

$$\begin{aligned} \mathbf{E}_e(k_{\text{eff}}, \mathbf{r}) &= \sum_n \left[q_n^e \mathbf{N}_n^{e(1)} - b_n^e \mathbf{N}_n^{e(3)} \right], \\ \mathbf{H}_e(k_{\text{eff}}, \mathbf{r}) &= \sum_n \frac{k_{\text{eff}}}{i\omega} \left\{ q_n^e \left[i\mu'_{ke} \mathbf{L}_n^{e(1)} + \mu'_{re} \mathbf{M}_n^{e(1)} \right] - b_n^e \left[i\mu'_{ke} \mathbf{L}_n^{e(3)} + \mu'_{re} \mathbf{M}_n^{e(3)} \right] \right\}, \end{aligned} \quad (5)$$

where the superscript e in q_n^e means k_{eff} is involved in VCWFs, μ'_{re} and μ'_{ke} are defined in Eq. (1).

By matching the standard boundary conditions at $r = r_0$, it can be obtained that

$$\begin{pmatrix} q_n^e \\ b_n^e \end{pmatrix} = \mathcal{F} \begin{pmatrix} \mathcal{A}_{11} & \mathcal{A}_{12} \\ \mathcal{A}_{21} & \mathcal{A}_{22} \end{pmatrix} \begin{pmatrix} q_n^0 \\ b_n^0 \end{pmatrix}, \tag{6}$$

with the prefactor $\mathcal{F} = \pi / (2i\mu_0\mu'_{re})$, and the matrix elements

$$\mathcal{A}_{11} = -x_0 J'_n(x_0) H_n^{(1)}(x_{\text{eff}}) + n\mu_0\mu'_{ke} J_n(x_0) H_n^{(1)}(x_{\text{eff}}) + x_{\text{eff}}\mu_0\mu'_{re} J_n(x_0) H_n^{(1)'}(x_{\text{eff}}), \tag{7a}$$

$$\mathcal{A}_{12} = x_0 H_n^{(1)'}(x_0) H_n^{(1)}(x_{\text{eff}}) - n\mu_0\mu'_{ke} H_n^{(1)}(x_0) H_n^{(1)}(x_{\text{eff}}) - x_{\text{eff}}\mu_0\mu'_{re} H_n^{(1)}(x_0) H_n^{(1)'}(x_{\text{eff}}), \tag{7b}$$

$$\mathcal{A}_{21} = -x_0 J'_n(x_0) J_n(x_{\text{eff}}) + n\mu_0\mu'_{ke} J_n(x_0) J_n(x_{\text{eff}}) + x_{\text{eff}}\mu_0\mu'_{re} J_n(x_0) J'_n(x_{\text{eff}}), \tag{7c}$$

$$\mathcal{A}_{22} = x_0 H_n^{(1)'}(x_0) J_n(x_{\text{eff}}) - n\mu_0\mu'_{ke} H_n^{(1)}(x_0) J_n(x_{\text{eff}}) - x_{\text{eff}}\mu_0\mu'_{re} H_n^{(1)}(x_0) J'_n(x_{\text{eff}}), \tag{7d}$$

with $x_0 = k_0 r_0$ and $x_{\text{eff}} = k_{\text{eff}} r_0$.

According to rule (iii) of the EMT, the coated rod located in the effective medium subjects to null scattering. According to the Mie theory, the total scattering cross section is $C_{\text{sca}} = 4\sum_n |D_n^e|^2 / k_{\text{eff}}$ with $D_n^e = b_n^e / q_n^e$ the Mie scattering coefficients of the coated rod in the effective medium. In the limit $k_{\text{eff}} r_0 \ll 1$, only the dominated terms of $n = 0, \pm 1$ need to be considered. Taking account of $D_n^e = b_n^e = 0$, it is straightforward from equation (6) to get

$$\frac{\mathcal{A}_{21}}{\mathcal{A}_{22}} = -\frac{b_n^0}{q_n^0} = -D_n^s, \quad n = 0, \pm 1, \tag{8}$$

where D_n^s are the Mie coefficients of the inner core ferrite rod, which are given by

$$D_n^s = \frac{k_0 r_s J_n(k_s r_s) J'_n(k_0 r_s) - \mu_0 J_n(k_0 r_s) j}{k_0 r_s H_n^{(1)'}(k_0 r_s) J_n(k_s r_s) - \mu_0 H_n^{(1)}(k_0 r_s) j}, \tag{9}$$

with $j = n\mu'_{ks} J_n(k_s r_s) + k_s r_s \mu'_{rs} J'_n(k_s r_s)$ where r_s is the radius of the inner core ferrite rod, μ'_{rs} and μ'_{ks} are given in Eq. (1). Suppose $k_{\text{eff}} r_0 \ll 1$ and $k_0 r_0 \ll 1$, we can make approximations on $J_n(x)$, $J'_n(x)$, $H_n^{(1)}(x)$, and $H_n^{(1)'}(x)$ with $x = k_{\text{eff}} r_0$ or $k_0 r_0$ for convenience.

Then we can obtain the simplified equations determining ϵ_{eff} and μ_{eff} .

$$\epsilon_{\text{eff}} = (1 - f)\epsilon_0 + f\tilde{\epsilon}_s, \quad \frac{\mu_{\text{eff}} - \mu_0}{\mu_{\text{eff}} + \mu_0} = f \frac{\tilde{\mu}_s - \mu_0 - \xi}{\tilde{\mu}_s + \mu_0 + \xi}, \tag{10}$$

where f is the filling fraction with $f = r_s^2 / r_0^2$, and

$$\tilde{\epsilon}_s = 2\epsilon_s F_2(x_s), \quad \tilde{\mu}_s = \mu_s G_2(x_s), \quad \xi = -\frac{(1 - f)\mu_0^2(\mu_\kappa / \mu_r)^2(\tilde{\mu}_s / \mu_s)^2}{(1 - f)\mu_0 + (1 + f)\tilde{\mu}_s}, \tag{11}$$

$$F_2(x_s) = J_1(x_s) / [x_s J_0(x_s)], \quad G_2(x_s) = J_1(x_s) / [x_s J'_1(x_s)],$$

with $x_s = k_s r_s$. It is noted that if μ_κ is set to be zero, equation (10) can be recovered to that for the isotropic case (Wu et al., 2006).

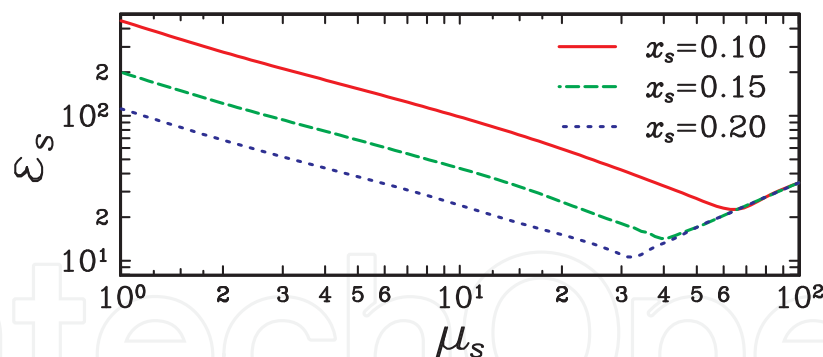


Fig. 9. Phase diagram for the 2D metamaterials composed of dielectric rods of radius r_s with respect to the permittivity ϵ_s and permeability μ_s . Above each curve the system may possess simultaneously negative magnetic and electric responses.

3.2 Simultaneous negative effective constitutive parameters obtained with EMT

We exemplify the ferrite-only-based designs with the 2D case, it is straightforward to generalize to the 3D case. We present in Fig. 9 the phase diagram of the system as a function of the permittivity ϵ_s and the permeability μ_s for the dielectric rods at a typical filling ratio $f = 0.385$. Above each curve is the region where the system may simultaneously display negative electric and magnetic responses within a certain frequency range that satisfies $x = (\omega/c)r_s \leq x_s$. Here ω is the angular frequency, r_s is the rod radius, and c is the speed of light in vacuum. As can be seen from the phase diagram, by employing ferrites with permeability over 10 as building block, the requisite permittivity can be lowered by an order of magnitude. In particular, the magnetically tunable permeability can serve to achieve manipulability of the operational frequency range and the wave impedance.

As a candidate of the ferrite materials, single-crystal yttrium-iron-garnet (YIG) can be the first choice for its negligible low damping $\alpha = 5 \times 10^{-4}$ (Poazar, 2004). The permeability of single-crystal YIG bears the same form as that given in Eq. (1) with the saturation magnetization $M_s = 1750$ Oe. In our proof-of-principle demonstration we set $\alpha = 0$ for convenience.

Based on the newly developed EMT, we have calculated the effective constitutive parameters of the MM. In Fig. 10(b) and (d) we present ϵ_{eff} and μ_{eff} as the functions of the angular frequency ω for an MM composed of ferrite rods arranged as a square lattice in the air with $a = 10$ mm, $r_s = 3.5$ mm, and $\epsilon_s = 25$. The exerted EMFs satisfy $H_0 = 500$ Oe and $H_0 = 475$ Oe, for the results shown in Fig. 10(b) and (d), respectively. It can be seen from Fig. 10(b) that within the frequency range from 15.5 GHz to 16.2 GHz, the system exhibits simultaneous negative ϵ_{eff} and μ_{eff} , implying a working frequency range for the NIM. To confirm the result, the corresponding photonic band diagrams are calculated by using the rigorous frequency-domain multiple scattering theory as shown in Fig. 10(a) and (c). Excellent agreement between two independent results is obtained. In particular, the working frequency of NIM corresponds to the second photonic band denoted by the blue line in Fig 10(a). At about 16.2 GHz, one gets a so-called epsilon-near-zero (ENZ) medium (Silveirinha & Engheta, 2006), which can induce a longitudinal EM mode in the system, corresponding to the nearly flat third band labeled by the black line in Fig. 10(a). The comparison between the band diagram and ϵ_{eff} and μ_{eff} confirms the validity of the CPA for the MM. A particularly important results obtained with the EMT is that at $\omega = 16$ GHz, the effective constitutive parameters $\epsilon_{\text{eff}} = \mu_{\text{eff}} = -1$ is realized as marked by the horizontal solid green line in Fig. 10(a) and (b).

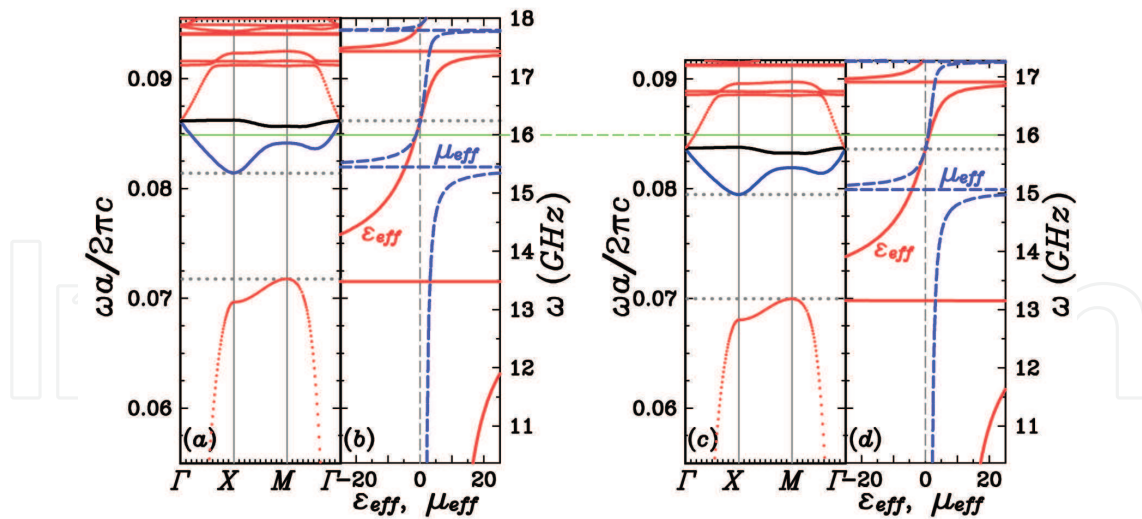


Fig. 10. (a) Photonic band diagram for an MM of square lattice with lattice constant $a = 10$ mm, rod radius $r_s = 3.5$ mm, and $H_0 = 500$ Oe. (b) Effective permittivity ϵ_{eff} and effective permeability μ_{eff} as the functions of circular frequency ω for the system with the same parameters as in (a). (c) and (d) are the same as (a) and (b) except $H_0 = 475$ Oe.

To demonstrate the manipulability of the negative refractive index by the EMF, we present in Fig. 10(d) ϵ_{eff} and μ_{eff} as the functions of ω at a smaller EMF such that $H_0 = 475$ Oe. The corresponding photonic band diagram is also given in Fig. 10(c). Good agreement can still be found for Fig. 10(c) and (d), which confirms once again the validity of the EMT. In addition, by comparing Fig. 10 (a) with (b) it can be found that the photonic band diagram is shifted to a lower frequency range, so does the operational frequency bandwidth of the NIM. At $\omega = 16$ GHz, the refractive index is no longer negative as can be seen from Fig. 10(d). Instead, it corresponds to the refractive index given by $n_{\text{eff}} = 1.13$ with $\epsilon_{\text{eff}} = 0.92$ and $\mu_{\text{eff}} = 1.4$. The operating frequency for the NIM is shifted downwards and located at about 15.5 GHz. Therefore, by appropriately adjusting the EMF, we can manipulate the working frequency for the NIM, which adds considerably to the flexibility in practical applications.

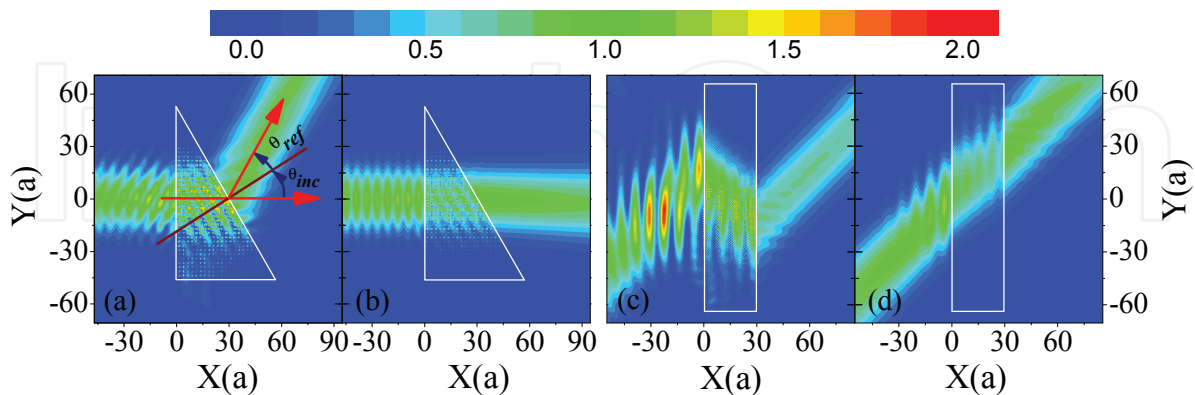


Fig. 11. A Gaussian beam incident on the MM with wedge and slab geometry experiences negative and positive refractions under the EMFs of $H_0 = 500$ Oe (a) and (c), and $H_0 = 475$ Oe (b) and (d), showing magnetic tunability from negative to positive refraction.

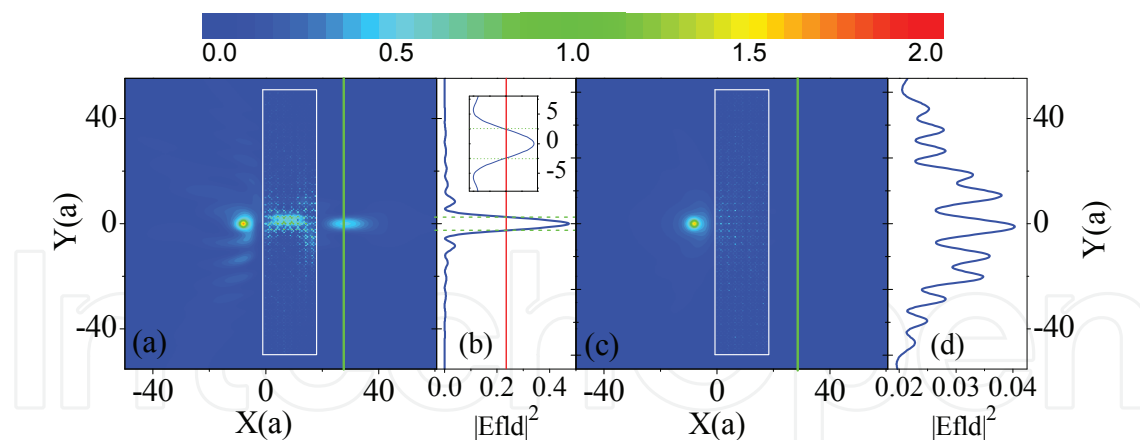


Fig. 12. Simulations on superlensing effect of an MM slab under the EMFs of $H_0 = 500$ Oe (a) and $H_0 = 475$ Oe (c). (b) and (d) demonstrate the intensity profiles along the solid green lines in (a) and (c), respectively. The inset in (b) is the amplified view of the image width at half maximum intensity, showing that the transverse image size is less than $\lambda/2$ for $H_0 = 500$ Oe.

3.3 Negative refraction controllable with a magnetic field

To corroborate the above theoretical design, we have performed simulations to examine the propagation of a TM Gaussian beam through a wedge-shaped MM under an EMF of $H_0 = 500$ Oe at the working frequency $\omega = 16$ GHz. The results are presented in Fig. 11(a) and (b). The beam shines on the interface normally from the left hand side and transmits through the wedge, as shown in Fig. 11(a). The incident angle at the wedge surface is $\theta_{\text{inc}} = \theta_0$ and the refraction angle is labeled as θ_{ref} . A negative refraction is clearly demonstrated in Fig. 11(a) with the refraction angle $\theta_{\text{ref}} \approx \theta_{\text{inc}}$, suggesting the effective refractive index $n_{\text{eff}} \approx -1$. Note in passing that only a very weak field appears at the bottom surface of the sample, suggesting that the Gaussian beam is subjected to a tiny reflection at the wedge surface, providing a persuasive evidence for the wave impedance match of the wedge-air interfaces. When H_0 is decreased to 475 Oe, the refractive index becomes positive from the CPA. The corresponding simulation result is shown in Fig. 11(b). The beam is seen to bend downwards a little bit, indicating a positive refraction, in agreement with the effective refractive index $n_{\text{eff}} = 1.13$ from the EMT.

The negative refraction behavior of the MM and its manipulability by the EMF can also be manifested by observing the propagation of a Gaussian beam through a flat slab. The results are typically presented in Fig. 11(c) and (d) for $H_0 = 500$ Oe and 475 Oe, respectively. A Gaussian beam, incident obliquely from the left hand side of the slab with incident angle $\theta_{\text{inc}} = 45^\circ$, is seen to refract negatively into the slab, with the refractive angle $\theta_{\text{ref}} \approx \theta_{\text{inc}}$. And then, it is subjected to another negative refraction at the right surface of the slab, as shown in Fig. 11(c), indicating once again the negative refractive behavior with $n_{\text{eff}} \approx -1$. One important thing to be noted is that at each interface of the slab we can hardly find the reflected beam, suggesting once again that effective permittivity ϵ_{eff} and effective permeability μ_{eff} are both nearly equal to -1 , resulting in the wave impedance match at the interface. The tunability of the negative refraction behavior is shown in Fig. 11(d), with $H_0 = 475$ Oe, where the beam transmits through the slab without obvious change of its direction, consistent with positive effective index $n_{\text{eff}} = 1.13$ from the CPA.

3.4 Subwavelength imaging controllable with a magnetic field

One of the most unique characteristics for the NIM is the slab superlensing effect (Pendry, 2000), which enables many potential applications. Typical slab imaging phenomena, together with its magnetic manipulability, based on our design of NIM is shown in Fig. 12, where the thickness of the slab is $t_s = 18a$. A monochromatic line source radiating EM waves at $\omega = 16$ GHz is placed at a distance $d_p = 8a$ from the left surface of the slab. When $H_0 = 500$ Oe, an image is formed on the opposite side of the slab with the image centered at a distance $d_i = 10.2a$ from the right surface of the slab, as shown in Fig. 12(a). The profile of the field intensity along the green line that goes through the image center in Fig. 12(a) is presented in Fig. 12(b), which corresponds to a transverse image size $w \lesssim 5a \approx 0.42\lambda$, demonstrating a possible subwavelength resolution below the conventional diffraction limit $\frac{1}{2}\lambda$. The separation d between the line source and the image is $d = d_p + d_i + t_s = 36.2a \approx 2t_s$, consistent with negative refractive index $n_{\text{eff}} = -1$ from EMT calculation. The manipulability of the EMF on the negative refractive index is exhibited in Fig. 12(c) and (d), where all the parameters are the same as those in Fig. 12(a) and (b) except that the EMF is taken as $H_0 = 475$ Oe instead of 500 Oe. As analyzed above, the refractive index is tuned from $n_{\text{eff}} = -1$ to a positive one with $n_{\text{eff}} = 1.13$. In this case, the slab shows no negative refraction behavior. For this reason, no image is formed on the opposite side of the slab as demonstrated in Fig. 12(c).

4. Molding the flow of EM wave with magnetic graded PC

PCs are composite materials with periodic optical index and characterized by anisotropic photonic band diagram and even PBG (Joannopoulos et al., 1995; John, 1987; Yablonovitch, 1987), enabling the manipulation of EM waves in novel and unique manners, paving the way to many promising applications. To achieve more degree of tunability, MPC with EM properties controllable by EMF has been proposed and investigated, which has ranged from photonic Hall effect (Merzlikin et al., 2005; Rikken & Tiggelen, 1996), extrinsic PCs (Xu et al., 2007), and giant magnetorefectivity (Lin & Chui, 2007) to magnetically tunable negative refraction (Liu et al., 2008; Rachford et al., 2007), magnetically created mirage (Chen et al., 2008), magnetically tunable focusing (Chen et al., 2008), and unidirectional waveguides (Haldane & Raghun, 2008; Wang et al., 2008; 2009; Yu et al., 2008). In previous research on PCs, most efforts are devoted to the PBG-relevant effects and its potential applications. Actually, the richness of the photonic bands of the PCs supplies to us more manipulability on the control of the EM wave. Of particular important paradigms are the negative refraction in PCs (Luo et al., 2002) and the superlensing effect based on it (Decoopman et al., 2006).

Graded PC is a kind of structured material constructed by introducing appropriate gradual modifications of some PC parameters such as the lattice periodicity (Centeno & Cassagne, 2005; Centeno et al., 2006), the filling factor (Chien & Chen, 2006), or the optical index. It can further modify the photonic dispersion bands or isofrequency curves of the PCs, and thus leads to some new ways of manipulability on the EM waves. In this section, we will propose and conceptualize an alternative type of graded PC: magnetic graded PC (MGPC). The photonic dispersion bands are tuned by applying a nonuniform EMF, instead of the gradual modification of the intrinsic parameters such as lattice periodicity or filling factor. To exemplify the idea of the MGPC and its applications, we present two proof-of-principle demonstrations in the following: one is the focusing effect by taking advantage of the MGPC, the other one is the mirage effect created by MGPC.

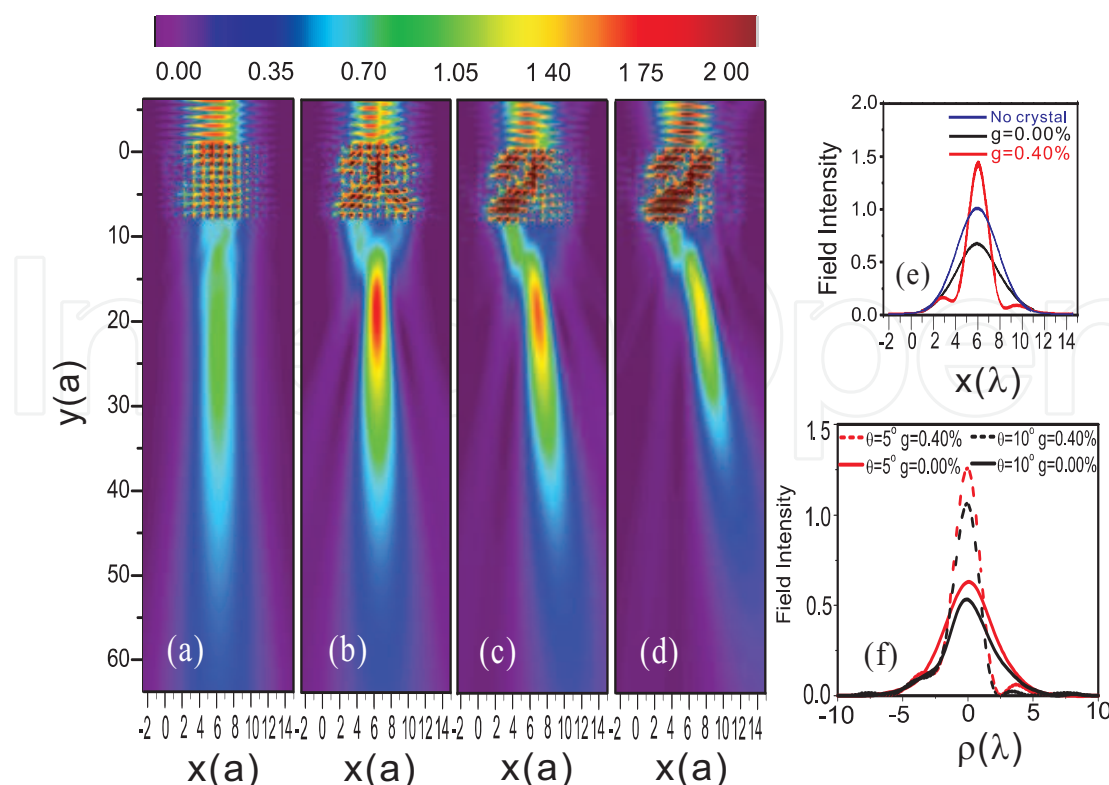


Fig. 13. The field pattern for an MGPC illuminated by a TM Gaussian incident from the top normally (a), (b) and obliquely (c), (d) with the gradient of the EMFs equal to $g = 0.00\%$ for (a) and $g = 0.4\%$ for (b), (c), and (d). The incident angle are $\theta = 5^\circ$ and $\theta = 10^\circ$ for (c) and (d), respectively. (e) and (f) are the field intensity at the focal plane as the functions of the abscissa x and distance from the focus ρ , respectively.

4.1 Subwavelength focusing effect based on magnetic graded PC

The MGPC proposed is composed of 117 (13 columns \times 9 rows) ferrite rods of radius $r_c = 6$ mm arranged periodically in the air as a square lattice with lattice constant $a = 48$ mm. For the EMF exerted along the z (rod axis) direction, the magnetic permeability of the ferrite rods is given in Eq. (1). With a slightly nonuniform EMF applied to the MPC, the permeability is gradually tuned, resulting in the modification of the refractive index, a graded PC is therefore obtained. The relative permittivity of the ferrite rod is $\epsilon_s = 12.3 + i3 \times 10^{-3}$, the saturation magnetization is $M_s = 1786$ Oe, and the damping coefficient is taken as 5×10^{-4} , typical for single-crystal YIG ferrite. We fix the Cartesian coordinates of the ferrite rods by $(x, y) = [(i - 1)a, (j - 1)a]$, with $i = 1, 2, \dots, 13$ and $j = 1, 2, \dots, 9$ the column and the row indices in x and y directions, respectively. The magnitude of the nonuniform EMF varies along the x direction, such that the EMF applied at the center region is weaker than that applied close to the edge of the MGPC sample. To be specific, the ferrite rod at the j -th row and the i -th column inside the MGPC is subjected to $H_0 = h_0[1 + (7 - i)g]$ for $i \leq 7$ and $H_0 = h_0[1 + (i - 7)g]$ for $i > 7$, where g is a parameter measuring the gradient of the EMF in x direction.

4.1.1 Focusing effect for a normally/obliquely incident TM Gaussian beam

Firstly, we consider the focusing effect of the MGPC on a collimated EM beam. In Fig. 13 (a) and (b), we present the field intensity pattern for the MGPC illuminated by a TM Gaussian beam. Figure 13(a) corresponds to the case when a uniform EMF in z direction is exerted

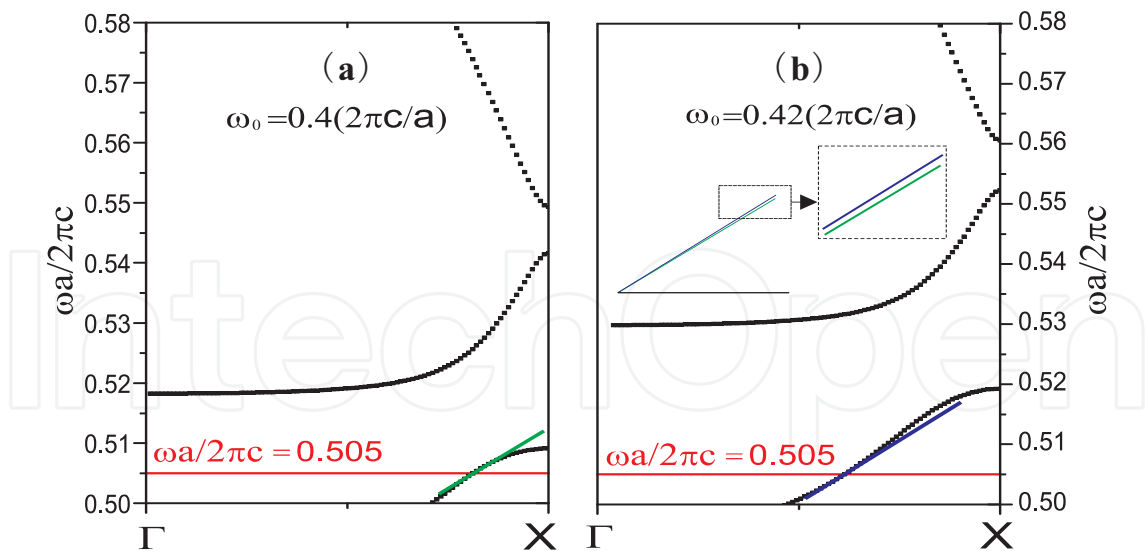


Fig. 14. Photonic band diagrams of the PC under two different uniform EMFs with $\omega_0 = 0.4(2\pi c/a)$ (a) and $\omega_0 = 0.42(2\pi c/a)$ (b). The green and blue lines are the tangents of the dispersion band at incident frequency $\omega = 0.505(2\pi c/a)$, shown also in the inset in Fig. 14(b).

so that one has a conventional MPC. It can be seen that the beam just transmits through the MPC without significant change of the beam waist radius, as can be seen from Fig. 13(e). When a slightly nonuniform EMF is exerted so that an MGPC is formed, the Gaussian beam is focused after passing through the MGPC, with the waist radius reduced to about half of the incoming beam, as demonstrated in Fig. 13(b) and (e), where the gradient g of the EMF is $g = 0.4\%$ and the Gaussian beam of waist radius $w_0 = 2\lambda$ is illuminated normally from the top of the MGPC with the wavelength λ ($a = 0.505\lambda$). We also present the results when the beam is obliquely incident on the MGPC, as shown in Fig. 13(c) and (d), corresponding to the incident angles of $\theta_i = 5^\circ$ and 10° , respectively. It can be found that the beam can still be focused. However, the intensity at the focus decreases with the increase of the incident angle as can be seen from Fig. 13(f), mainly due to the stronger reflection for the larger incident angle at the interface. It should be pointed out that the weak gradient (with $g < 0.7\%$ in all cases) of the EMF and the small ferrite rod radius ($r_c = \frac{1}{8}a$) allow us to assume that each rod is subjected to a uniform EMF. Within this approximation, the simulations can be performed by using the multiple scattering method (Liu & Lin, 2006; Liu et al., 2008).

4.1.2 Physical understanding of the effect from the aspect of photonic band diagram

The focusing effects observed above can be understood using the concept of the local photonic band diagram as in the case of the conventional graded PC. In Fig. 14, we plot the photonic band diagram for the PC subjected to two different uniform EMFs where ω is the circular frequency of the incident EM beam. It can be seen that the photonic band diagram exhibits a noticeable difference when the magnitude of the EMF is slightly changed. At $\omega a/2\pi c = 0.505$, it can be seen from the inset in Fig. 14(b) that the slope of the photonic band is larger under the greater EMF. With the knowledge that $d\omega/dk \propto 1/n$ (n the effective optical index), the greater EMF produces the smaller optical index. Therefore, it can be understood that the gradient of the EMF yields a gradient optical index, leading to the formation of the MGPC.

We now further examine the magnetic tunability of the MGPC on the EM Gaussian beam. Firstly, we consider the effect of the number of rows m_r on the light focusing. In Fig. 15(a)

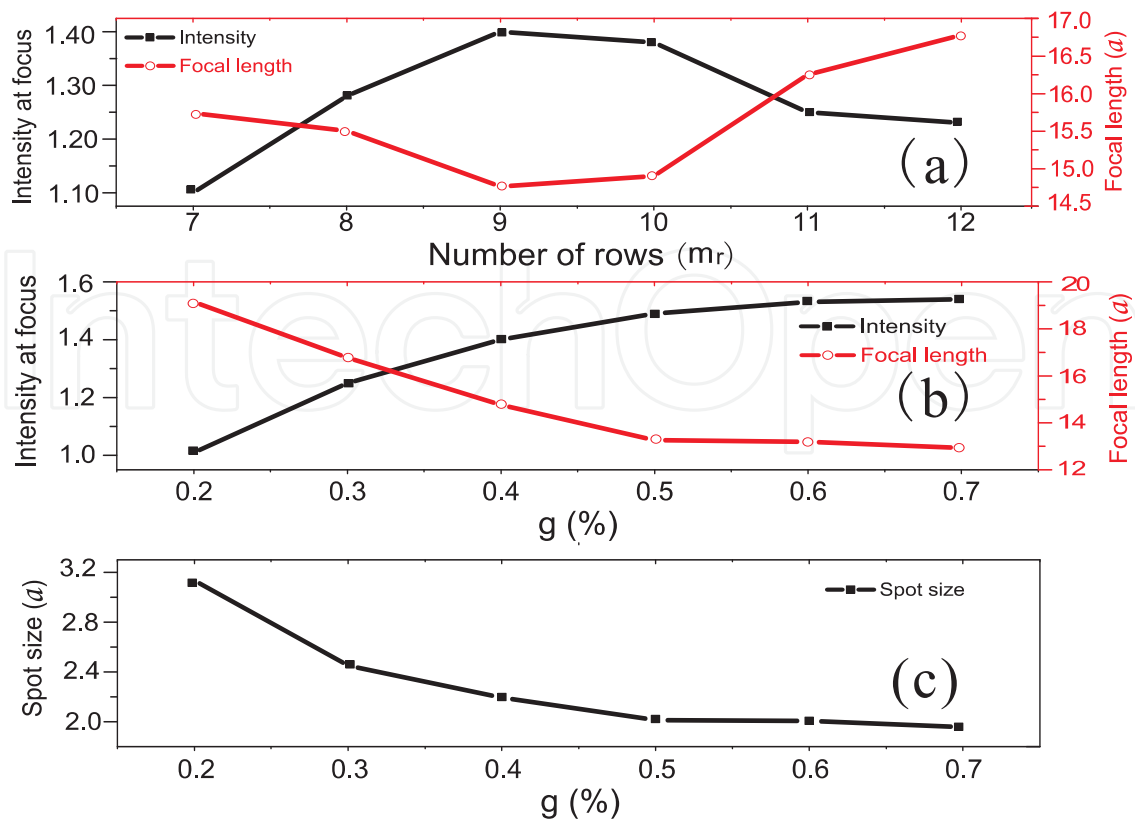


Fig. 15. The field intensity at the focus and the focal length as the functions of the number m_r of rows (a) and the gradient g of the EMF (b). (c) The waist radius of the focused beam versus the gradient g of the EMF. The number of columns is $m_c = 13$ and $g = 0.40\%$ for (a).

we present the focal length and the intensity at the focus versus m_r . It can be seen that the intensity at the focus increases at first with the increase of m_r , and reaches its maximum at $m_r = 9$. This is because the more rows the light beam goes across, the more focusing effect it will experience. As m_r increase further, the intensity at the focus decreases, due to the damping occurring when the light propagates through the MGPC. We also examine the effect of the gradient g of the EMF on the focusing property. It can be seen from Fig. 15(b) that the intensity at the focus increases with the increase of g . At $g = 0.7\%$, the intensity is twice as that for the MGPC under the uniform EMF. In addition, the focal length decreases as g increases, ranging from $13a$ to $19a$. From Fig. 15(c), it can be seen that the spot size decreases as g increases, and shrinks even to $1.5a$ at $g = 0.70\%$, less than the wavelength of the incident wave. The effect of tuning the gradient g bears a close similarity to the case of modifying the curvature or the central thickness of the conventional lens in classical optics, demonstrating the magnetical tunability of the MGPC on the focusing properties.

4.2 Tunable mirage effect based on magnetic graded PC

The MGPC considered is composed of 20 rows and 80 columns of 1600 ($80 \text{ columns} \times 20 \text{ rows}$) ferrite rods arranged periodically in the air as a square lattice. The ferrite rod has the same parameters as in the last section. The lattice constant is still $a = 48 \text{ mm} = 8r_c$. The Cartesian coordinates of the rods are given by $(x, y) = [(i - 1)a, (j - 1)a]$, with $i = 1, 2, \dots, 80$ and $j = 1, 2, \dots, 20$ labeling the column and row indices in x and y directions, respectively. An EMF oriented along z with the gradient in y direction is exerted upon the MGPC such that the

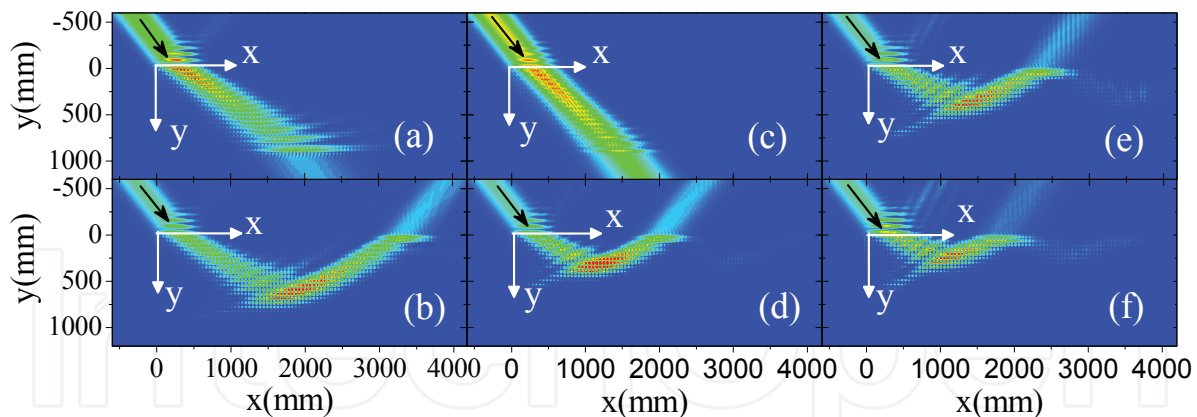


Fig. 16. Field intensity patterns for an MGPC illuminated by a TM Gaussian beam with wavelength $\lambda = 91.427$ mm for panel (f) and $\lambda = 90.564$ mm for other panels. The black arrows denote the direction of the incident beam. The MGPC-air interfaces are located at $y = -24$ mm and $y = 936$ mm. The applied EMFs exerted satisfy that (a) $h_0 = 893$ Oe, $g = 0.00\%$; (b) $h_0 = 893$ Oe, $g = 0.23\%$; (c) $h_0 = 848$ Oe, $g = 0.00\%$; (d) $h_0 = 893$ Oe, $g = 0.40\%$; (e) $h_0 = 904$ Oe, $g = 0.23\%$; and (f) $h_0 = 893$ Oe, $g = 0.23\%$.

ferrite rod in the j -th row and i -th column is subjected to magnetic field $H_0 = h_0[1 + (j - 1)g]$ with g the quantity measuring the amplitude of the gradient. The incident EM wave is the TM Gaussian beam with the waist radius $w_0 = 3\lambda$, where λ is the wavelength of the beam in vacuum.

4.2.1 Creating a mirage effect for a TM Gaussian beam based on an MGPC

In Fig. 16, we present the electric field intensity patterns for an MGPC under different EMFs illuminated by an incident TM Gaussian beam with the incident angle $\theta_{inc} = 45^\circ$. It can be seen that the beam is deflected in different manners with different EMFs exerted upon the MGPC. When a uniform EMF with gradient $g = 0$ is applied, the MGPC is actually an ordinary MPC. It can be seen from Fig. 16(a) that in this case the beam enters the MGPC at $y = -24$ mm with a refraction angle greater than 45° and finally transmits across the crystal. Very differently, when a slight gradient is introduced to the EMF such that $g = 0.23\%$, the beam is deflected layer by layer during its propagation in the MGPC and eventually reflected back off the MGPC, leading to the appearance of a mirage effect as shown in Fig. 16(b).

4.2.2 Physical understanding of the effect from the aspect of isofrequency curve

In nature, a mirage is an optical phenomenon occurring when light rays bend and go along a curved path. The reason lies in the gradual variation of the optical index of air, arising from the change of the atmosphere temperature with the height. Roughly speaking, in our case the nonuniform EMF produces a similar effect on the effective refractive index of the MGPC as the temperature does on the atmosphere, so that an mirage effect is created. More exact analysis relies on the isofrequency (IF) curves of the MPC (Kong, 1990). Due to the weak gradient of the EMF (less than 0.5%) in all our simulations, the propagation of the EM wave can be interpreted according to the local dispersion band or the IF curve (Centeno et al., 2006). In Fig. 17(a), we present three IF curves for the operating wavelength $\lambda = 90.564$ mm, corresponding to the MPC under three different uniform EMFs (with $g = 0$). The blue vertical line in Fig. 17(a) denotes parallel component of the wavevector for the incident EM wave. According to the conservation of tangential wavevector at the MPC-air interface, the parallel

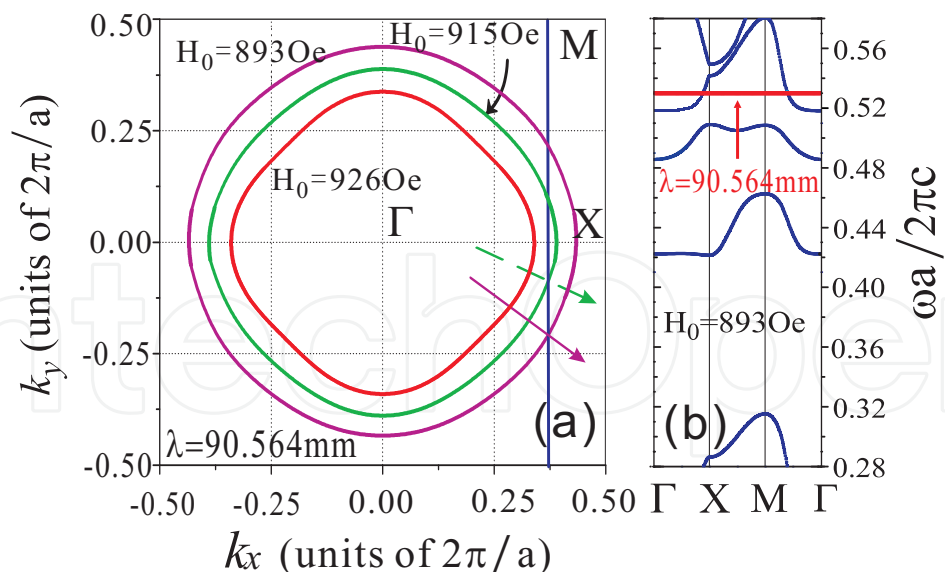


Fig. 17. (a) Isofrequency curves corresponding to the wavelength $\lambda = 90.564$ mm of the MPC under three different EMFs. The straight arrows denote the direction of the group velocity. The blue vertical line in Fig. 17 (a) is the construction line corresponding to an incident angle of 45° , obtained by the conservation of tangential momentum at the interface. (b) Photonic band diagram of the MPC under $H_0 = 893$ Oe.

wavevector of the refracted EM wave in the MPC can be obtained. Then the refractive angle can be determined by the surface normal at the intersection point of the IF curve and the blue vertical line, as marked by the blue solid and green dashed arrows in Fig. 17(a), corresponding to the direction of the group velocities $V_g = \nabla_k \omega(k)$ in the MPC under $H_0 = 893$ and 915 Oe, respectively. For convenience, we also present in Fig. 17(b) the photonic band diagram of an MPC under $H_0 = 893$ Oe, where the red solid line marks the operating frequency in Fig. 17(a). As we have shown in the previous section, the increase of the EMF will result in the shift of the photonic bands to higher frequency. Correspondingly, the IF curves will shrink with the increase of the EMF as can be seen from Fig. 17(a), resulting in the increase of the refraction angle by comparing the blue solid arrow with green dashed arrow.

The above analysis based on the IF curves and the photonic band diagram can be corroborated by comparing Figs. 16(a) ($H_0 = 893$ Oe) with 16(c) ($H_0 = 848$ Oe), where a stronger EMF corresponds to a larger refraction angle. Accordingly, a gradient EMF enables a continuous change of refraction angle of the beam propagating in the MGPC. A typical result is shown in Fig. 16(b) where an EMF with gradient $g = 0.23\%$ is applied. It can be seen that as the beam goes deeper and deeper into the MGPC, the refraction angle will increase layer by layer in the MGPC due to the increase of the EMF along the y direction. Physically, with the increases of EMF along y , the local IF shrinks little by little until it becomes tangent to the vertical construction line. This occurs when H_0 lies between 915 Oe and 926 Oe, as illustrated in Fig. 17(a), leading to a total internal reflection. The beam is therefore reflected back, resulting in a mirage effect.

To examine the sensitivity of the mirage effect to the gradient g of the EMF and the wavelength of the incident beam, we present in Fig. 19 the separation d_s between the incoming and outgoing beam as their functions. The separation d_s characterizes the degree of bending for the mirage effect. In Fig. 19(a) it can be found that d_s decrease as the gradient increases, which can also be observed by comparing Figs. 16(b) and (d), indicating a stronger bending by a

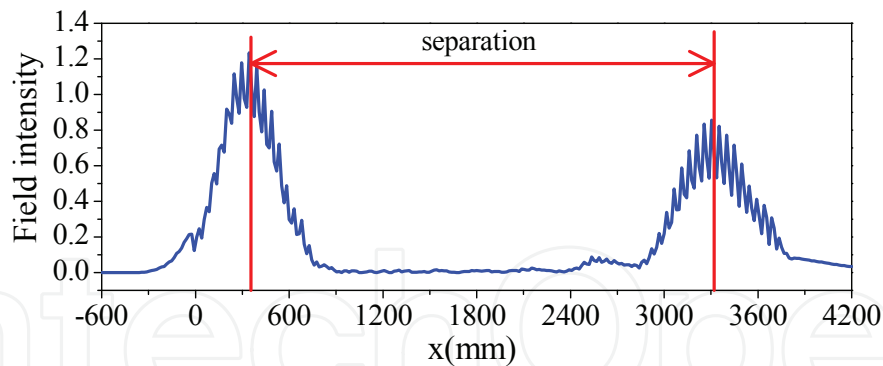


Fig. 18. The field intensity at the top of the MGPC for the case shown in Fig. 16(b).

higher gradient EMF. In addition, from Fig. 19(b) it can be seen that the separation exhibits a sensitive dependence on the incident wavelength, which is also demonstrated by comparing Figs. 16(b) and (f), suggesting a possible application in multiplexer and demultiplexer.

5. Unidirectional reflection behavior on magnetic metamaterial surface

Magnetic materials are irreplaceable ingredients in optical devices such as isolators and circulators. Different from dielectric or metallic materials, the permeability of magnetic material is a second rank tensor with nonzero off-diagonal elements as given in Eq. (1). Accordingly, the time reversal symmetry is broken in a MM system (Wang et al., 2008), based on which some very interesting phenomena can be realized. A particular one is the one-way edge state which has been investigated theoretically (Chui et al., 2010; Haldane & Raghu, 2008; Wang et al., 2008; Yu et al., 2008) and experimentally (Wang et al., 2009) recently. Besides, MSP resonance occurs in MPC when effective permeability equals to -1 in 2D case, in the vicinity of which the behavior of MM is very different, it is therefore the frequency region we will focus on.

In magnetic systems with inversion symmetry, even though the dispersion is symmetric, the wave functions for opposite propagating directions can become asymmetric. For this reason, the reflected wave develops a finite circulation, specially near the MSP resonance frequency, it can be substantially amplified. This effect can be exploited to construct one-way subwavelength waveguides that exhibit a superflow behavior. In this section, our work

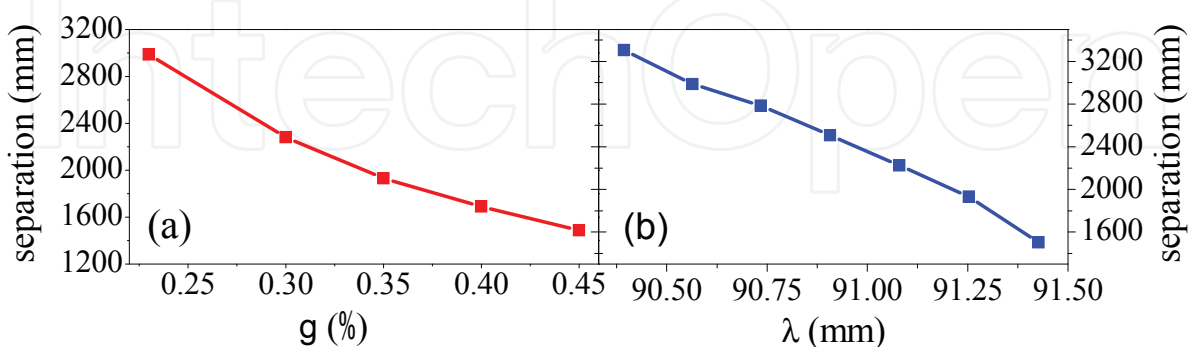


Fig. 19. The peak separation is plotted as the function of the field gradient g (a) and the incident wavelength λ (b). The other parameters are the same as those in Fig. 16(b). The separation d_s can be determined from the field intensity distribution along the x axis at $y = 0$, as is illustrated in Fig. 18 for parameters corresponding to those in Fig. 16(b).

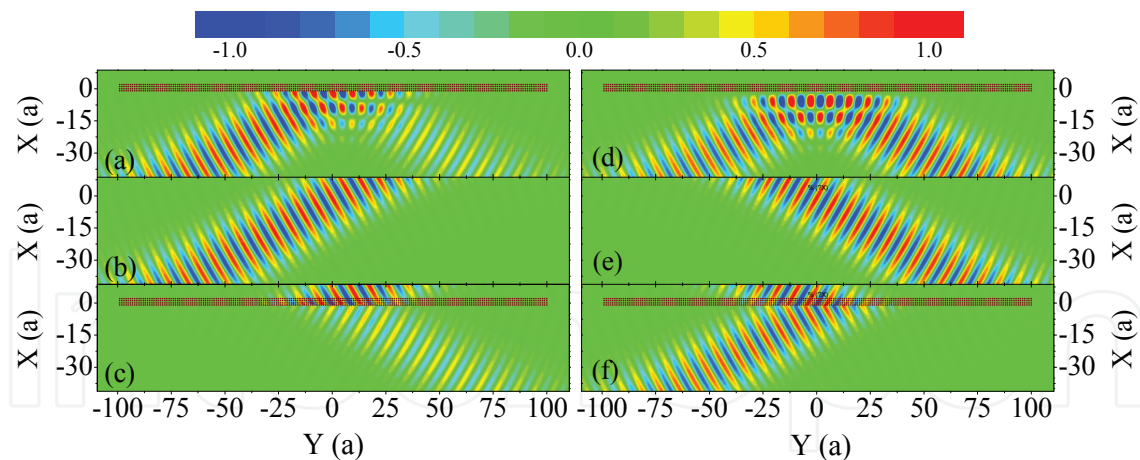


Fig. 20. The electric field pattern of the total field (a), (d), the incoming field (b), (e), and the scattered field (c), (f) for a TM Gaussian beam incident from left hand side (incident angle $\theta_{inc} = 60^\circ$) and right hand side (incident angle $\theta_{inc} = -60^\circ$) upon a four-layer MM slab. The positions of the ferrite rods are marked by the black dot.

is devoted to understanding the mechanism of this “finite circulation” and its physical consequence.

5.1 Unidirectional reflection of an EM Gaussian beam from an MM surface

The MM considered is composed of an array of ferrite rods arranged periodically in the air as a square lattice with the lattice constant $a = 8$ mm. The ferrite rod has the radius $r = 0.25a = 2$ mm. The permittivity of the ferrite rod $\epsilon_s = 12.6 + i7 \times 10^{-3}$. The magnetic susceptibility tensor is of the same form as that given by Eq. (1). Here, the saturation magnetization is $4\pi M_s = 1700$ Oe and the EMF is fixed so that $H_0 = 900$ Oe, corresponding to the MSP resonance frequency $f_s = \frac{1}{2\pi}\gamma(H_0 + 2\pi M_s) = 4.9$ GHz with γ the gyromagnetic ratio. The damping coefficient is $\alpha = 7 \times 10^{-3}$, typical for the NiZn ferrite.

By use of the multiple scattering method, we demonstrate the reflection behavior of a TM Gaussian beam reflected from a finite four-layer MM slab with each layer consisting of 200 ferrite rods. We have examined the cases of the incoming Gaussian beams with incident angles of $\pm 60^\circ$. The beam center is focused on the middle (100-th) ferrite rod in the first layer. The working frequency is fixed as $f_w = 4.84$ GHz, located in the vicinity of the MSP resonance. The results are illustrated in Fig. 20 where we present the electric field patterns of the Gaussian beams with opposite components of wavevector parallel to the MM slab. For the Gaussian beam incident from the left hand side, the reflected wave is very weak as shown in Fig 20(a). However, for the Gaussian beam incident from the right hand side, the intensity of the reflected wave remains substantial as shown in Fig 20(d). It is evident that there exists remarkable difference for the reflected Gaussian beams at different directions. The similar behavior can also be observed for a line source close to the MM slab where the reflection nearly disappears on one side of the line source.

5.2 Scattering amplitude corresponding to different angular momenta

The MM slab considered in our calculation is a geometrically left-right symmetric sample and the bulk photonic band are also the same for the above two incoming directions. Our effect arises from the characteristic of the wave functions at the working frequency. To gain a deeper understanding of our results, we calculate the scattering amplitudes corresponding

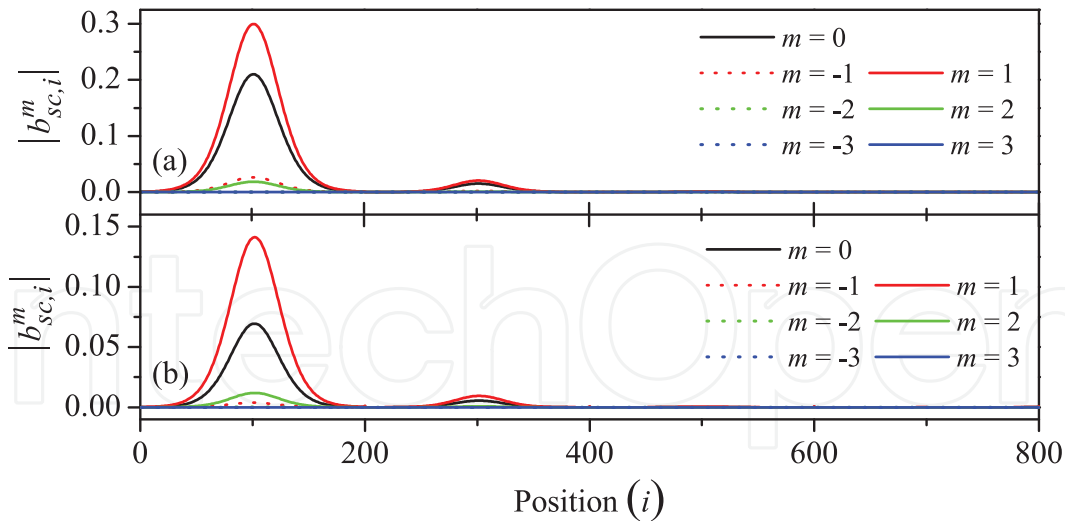


Fig. 21. The scattering amplitude $|b_{sc,i}^m|$ of different angular momenta at rod i for an incoming Gaussian beam with incident angle of $\theta_{inc} = 60^\circ$ (a) and -60° (b). Labels 1-200, 201-400, 401-600, and 601-800 correspond to the first, second, third, and fourth layers.

to different angular momenta $|b_{sc,i}^m|$ at the sites of different rods i in the MM slab. The results are shown in Fig. 21(a) and (b), corresponding to the cases of incident angles equal to 60° and -60° , respectively. As can be found from Fig. 21(a) for $\theta_{inc} = 60^\circ$, only the components of positive angular momenta m (0 and 1) are dominant, while all the other components are nearly suppressed. The result is absolutely different from the usual case that the scattering amplitudes of the opposite angular momenta are equal and that corresponding to angular momentum 0 is the largest. The similar behavior also exist for the opposite incoming direction as shown in Fig. 21(b), however, the amplitude is relatively weaker. Actually, the behavior originates from the breaking of the time-reversal symmetry, which support the energy flow only in one direction. In the vicinity of the MSP resonance the effect is intensified so that we can observe the sharply asymmetric reflection demonstrated in Fig. 20.

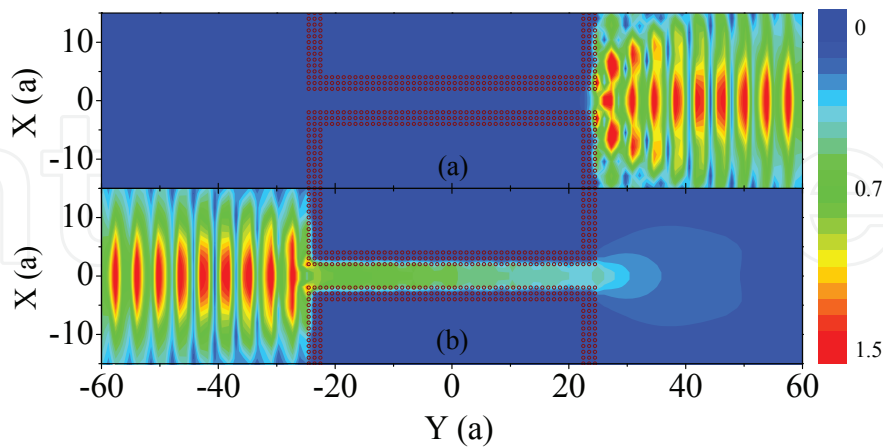


Fig. 22. The electric field patterns of a Gaussian beam incident along the channel with the width equal to $4a$. The Gaussian beam can pass the channel for one direction (b), while for the opposite direction it is completely suppressed (a).

5.3 Design of a possible EM device based on the effect

Finally, we demonstrate a potential application of our effect by constructing a unidirectional waveguide composed of two MM slabs of opposite magnetizations. A typical result is illustrated in Fig. 22 where the electric field patterns of a Gaussian beam incident along an interconnect/waveguide with the width of the channel equal to $4a$ are simulated. Due to the impedance mismatch at the interface, the field inside is less than that outside. Once inside, the Gaussian beam can pass the channel for one direction, while for the opposite direction it is completely suppressed. It should be pointed out that the damping coefficient in our design is twenty times larger than that used in the previous design by Wang and coworkers (Wang et al., 2008). While the transmission field still has an adequate intensity, which make it more applicable.

6. Conclusion

In summary, we have considered a kind of structured material which can be used to manipulate the flow of EM wave with much more flexibilities than conventional dielectrics. Firstly, a PBG material with robust and completely tunable photonic gap is designed and analyzed. Then, we design a ferrite-based negative index metamaterial with effective constitutive parameters $\epsilon_{\text{eff}} = \mu_{\text{eff}} = -1$. In addition, the corresponding EM property can be manipulated by an external magnetic field. After that, we propose an alternative type of graded PC, a magnetic graded PC, formed by a nonuniform external magnetic field exerted on an MPC, based on which a focusing effect and a mirage effect can be created and tuned. In the end, we demonstrate an exotic reflection behavior of a Gaussian beam from an MM slab, arising from the breaking of time reversal symmetry and the MSP resonance.

Based on the fast switching effect of the phenomena observed above, we can expect many promising applications such as a band filter, a multiplexer/demultiplexer, slab superlens, unidirectional waveguide, beam bender, and beam splitter with manipulability by an external magnetic field. Besides, we have also developed a set of theory for the calculations of band diagram, effective constitutive EM parameters, and electric field pattern. However, what we have considered is just for the two dimensional case. Generalization to three dimension will make the theory and the designed electromagnetic devices more applicable. Another matter should be mentioned is that the working frequency of the magnetic metamaterials is in the microwave region. In our future work, we will try to extend our design to higher frequency.

7. Acknowledgements

This work is supported by the China 973 program (2006CB921706), NNSFC (10774028, 10904020), MOE of China (B06011), SSTC (08dj1400302), China postdoctoral science foundation (200902211), and Zhejiang Normal University initiative foundation. STC is partly supported by the DOE.

8. References

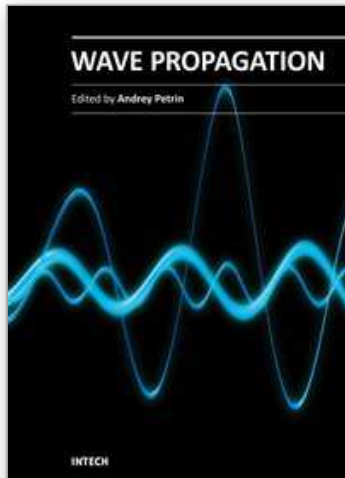
- Busch, K. & John, S. (1999). Liquid-crystal photonic-band-gap materials: The tunable electromagnetic vacuum. *Phys. Rev. Lett.*, Vol. 83, No. 05, 967-970
- Centeno, E. & Cassagne, D. (2005). Graded photonic crystals. *Opt. Lett.*, Vol. 30, No. 17, 2278-2280
- Centeno, E.; Cassagne, D. & Albert, J. P. (2006). Mirage and superbending effect in two-dimensional graded photonic crystals. *Phys. Rev. B.*, Vol. 73, No. 23, 235119

- Chan, C. T.; Yu, Q. L. & Ho, K. M. (1995). Order-N spectral method for electromagnetic waves. *Phys. Rev. B*, Vol. 51, No. 23, 16635-16642
- Chen, X.; Grzegorzczak, T. M.; Wu, B. I.; Pacheco, J. & Kong, J. A. (2004). Robust method to retrieve the constitutive effective parameters of metamaterials. *Phys. Rev. E*, Vol. 70, No. 1, 016608
- Chen, P.; Wu, R. X.; Xu, J.; Jiang, A. M. & Ji, X. Y. (2007). Effects of magnetic anisotropy on the stop band of ferromagnetic electromagnetic band gap materials. *J. Phys.: Condens. Matter*, Vol. 19, No. 10, 106205
- Chen, S. W.; Du, J. J.; Liu, S. Y.; Lin, Z. F. & Chui, S. T. (2008). Molding the flow of electromagnetic wave and creating mirage with a magnetic field. *Phys. Rev. A*, Vol. 78, No. 4, 043803
- Chen, S. W.; Du, J. J.; Liu, S. Y.; Lin, Z. F. & Chui, S. T. (2008). Focusing the electromagnetic wave with a magnetic field. *Opt. Lett.*, Vol. 33, No. 21, 2476-2478
- Chien, H. T. & Chen, C. C. (2006). Focusing of electromagnetic waves by periodic arrays of air holes with gradually varying radii. *Opt. Express*, Vol. 14, No. 22, 10759-10764
- Chui, S. T.; Liu, S. Y. & Lin Z. F. (2010). Reflected wave of finite circulation from magnetic photonic crystals. *J. Phys.: Condens. Matter*, Vol. 22, No. 18, 182201
- Decoopman, T.; Tayeb, G.; Enoch, S.; Maystre, D. & Gralak B. (2006). Photonic crystal lens: From negative refraction and negative index to negative permittivity and permeability. *Phys. Rev. Lett.*, Vol. 97, No. 7, 073905
- Dolling, G.; Enkrich, C.; Wegener, M.; Soukoulis, C. M. & Linden, S. (2006). Simultaneous Negative Phase and Group Velocity of Light in a Metamaterial. *Science*, Vol. 312, No. 5775, 892-894
- Figotin, A.; Godin, Y. A. & Vitebsky, I. (1998). Two-dimensional tunable photonic crystals. *Phys. Rev. B*, Vol. 57, No. 5, 2841-2848
- Golosovsky, M.; Saado, Y. & Davidov, D. (1999). Self-assembly of floating magnetic particles into ordered structures: A promising route for the fabrication of tunable photonic band gap materials. *Appl. Phys. Lett.*, Vol. 75, No. 26, 4168-4170
- Haldane, F. D. M. & Raghu, S. (2008). Possible realization of directional optical waveguides in photonic crystals with broken time-reversal symmetry. *Phys. Rev. Lett.*, Vol. 100, No. 1, 013904
- Halevi, P. & Ramos-Mendieta, F. (2000). Tunable photonic crystals with semiconducting constituents. *Phys. Rev. Lett.*, Vol. 85, No. 9, 1875-1878
- Ho, K. M.; Chan, C. T. & Soukoulis, C. M. (1990). Existence of a photonic gap in periodic dielectric structures. *Phys. Rev. Lett.*, Vol. 65, No. 25, 3152-3155
- Hu, X. H.; Chan, C. T.; Zi, J.; Li, M. & Ho, K. M. (2006). Diamagnetic response of metallic photonic crystals at infrared and visible frequencies. *Phys. Rev. Lett.*, Vol. 96, No. 22, 223901
- Hu, X. H.; Ho, K. M.; Chan, C. T. & Zi, J. (2008). Homogenization of acoustic metamaterials of Helmholtz resonators in fluid. *Phys. Rev. B*, Vol. 77, No. 17, 172301
- Inoue, M.; Fujikawa, R.; Baryshev, A.; Khanikaev, A.; Lim, P. B.; Uchida, H.; Aktsipetrov, O.; Fedyanin, A.; Murzina, T. & Granovsky, A. (2006). Magnetophotonic crystals. *J. Phys D*, Vol. 39, No. 8, R151-R161
- Jin, J. J.; Liu, S. Y.; Lin, Z. F. & Chui, S. T. (2009). Effective-medium theory for anisotropic magnetic metamaterials. *Phys. Rev. B*, Vol. 80, No. 11, 115101
- Joannopoulos, J. D.; Meade, R. D. & Winn, J. N. (1995). *Photonic Crystals*, NJ: Princeton University Press, Princeton.

- John, S. (1987). Strong localization of photons in certain disordered dielectric superlattices. *Phys. Rev. Lett.*, Vol. 58, No. 23, 2486-2489
- Kang, D.; Maclennan, J. E.; Clar, N. A.; Zakhidov, A. A. & Baughman, R. H. (2001). *Phys. Rev. Lett.*, Vol. 86, No. 18, 4052-4055
- Kee, C. S.; Kim, J. E.; Park, H. Y. & Lim, H. (2000). Two-dimensional tunable magnetic photonic crystals. *Phys. Rev. B*, Vol. 61, No.23, 15523-15525
- Kee, C. S. & Lim, H. (2001). Tunable complete photonic band gaps of two-dimensional photonic crystals with intrinsic semiconductor rods. *Phys. Rev. B*, Vol. 64, No. 12, 121103
- Kim, S. & Gopalan, V. (2001). Strain-tunable photonic band gap crystals. *Appl. Phys. Lett.*, Vol. 78, No. 20, 3015-3017
- Kong, J. A. (1990). *Electromagnetic Wave Theory*, Wiley, New York.
- Koschny, T.; Markoš, P.; Smith, D. R. & Soukoulis, C. M. (2003). Resonant and antiresonant frequency dependence of the effective parameters of metamaterials. *Phys. Rev. E*, Vol. 68, No. 6, R065602
- Koschny, T.; Markoš, P.; Economou, E. N.; Smith, D. R.; Vier, D. C. & Soukoulis, C. M. (2005). Impact of inherent periodic structure on effective medium description of left-handed and related metamaterials. *Phys. Rev. B*, Vol. 71, No. 24, 245105
- Kuzmiak, V.; Maradudin, A. A. & Pincemin, F. (1994). Photonic band structures of two dimensional systems containing metallic components. *Phys. Rev. B*, Vol. 50, No. 23, 16835-16844
- Leonhardt, U. (2006). Optical conformal mapping. *Science*, Vol. 312, No. 5781, 1777-1780
- Li, L. M. & Zhang, Z. Q. (1998). Multiple-scattering approach to finite-sized photonic band-gap materials. *Phys. Rev. B*, Vol. 58, No. 15, 9587-9590
- Lin, Z. F. & Chui, S. T. (2004). Electromagnetic scattering by optically anisotropic magnetic particle. *Phys. Rev. E*, Vol. 69, No. 5, 056614
- Lin, Z. F. & Chui, S. T. (2007). Manipulating electromagnetic radiation with magnetic photonic crystals. *Opt. Lett.*, Vol. 32, No. 16, 2288-2290
- Liu S. Y. & Lin, Z. F. (2006). Opening up complete photonic bandgaps in three-dimensional photonic crystals consisting of biaxial dielectric spheres. *Phys. Rev. E*, Vol. 73, No. 6, 066609
- Liu, S. Y.; Du, J. J.; Lin, Z. F.; Wu, R. X. & Chui S. T. (2008). Formation of robust and completely tunable resonant photonic band gaps. *Phys. Rev. B*, Vol. 78, No. 15, 155101
- Liu, S. Y.; Chen, W. K.; Du, J. J.; Lin, Z. F.; Chui, S. T. & Chan, C. T. (2008). Manipulating negative-refractive behavior with a magnetic field. *Phys. Rev. Lett.*, Vol. 101, No. 15, 157407
- Luo, C.; Johnson, S. G.; Joannopoulos, J. D. & Pendry, J. B. (2002). All-angle negative refraction without negative effective index. *Phys. Rev. B*, Vol. 65, No. 20, R201104
- Lyubchanskii, I. L.; Dadoenkova, N. N.; Lyubchanskii, M. I.; Shapovalov, E. A. & Rasing, Th. (2003). Magnetic photonic crystals. *J. Phys. D*, Vol. 36, No. 18, R277-R287
- Maier, S. A.; Kik, P. G. & Atwater H. A. (2002). Observation of coupled plasmon-polariton modes in Au nanoparticle chain waveguides of different lengths: Estimation of waveguide loss. *Appl. Phys. Lett.*, Vol. 81, No. 9, 1714-1716
- Maier, S. A.; Kik, P. G.; Atwater, H. A.; Meltzer, S.; Harel, E.; Koel, B. E. & Requicha, A. A. G. (2003). Local detection of electromagnetic energy transport below the diffraction limit in metal nanoparticle plasmon waveguides. *Nature Mater.*, Vol. 2, No.4, 229-232
- McGurn, A. R. & Maradudin, A. A. (1993). Photonic band structures of two and three

- dimensional periodic metal or semiconductor arrays. *Phys. Rev. B*, Vol. 48, No. 23, 17576-17579
- Merzlikin, A. M.; Vinogradov, A. P.; Inoue, M. & Granovsky, A. B. (2005). Giant photonic Hall effect in magnetophotonic crystals. *Phys. Rev. E*, Vol. 72, No. 4, 046603
- Modinos, A.; Yannopapas, V. & Stefanou, N. (2000). Scattering of electromagnetic waves by nearly periodic structures. *Phys. Rev. B*, Vol. 61, No. 12, 8099-8107
- Moroz, A. (2002). Metallo-dielectric diamond and zinc-blende photonic crystals. *Phys. Rev. B*, Vol. 66, No. 11, 115109
- Pendry, J. B.; Holden, A. J.; Stewart, W. J. & Youngs, I. (1996). Extremely low frequency plasmons in metallic mesostructures. *Phys. Rev. Lett.*, Vol. 76, No. 25, 4773-4776
- Pendry, J. B.; Holden, A. J.; Holden, D. J. & Stewart, W. J. (1999). Magnetism from conductors and enhanced nonlinear phenomena. *IEEE Tran. Microwave Theory Tech.*, Vol. 47, No. 11, 2075-2084
- Pendry, J. B. (2000). Negative refraction makes a perfect lens. *Phys. Rev. Lett.*, Vol. 85, No. 18, 3966-3969
- Pendry, J. B.; Schurig, D. & Smith, D. R. (2006). Controlling electromagnetic fields. *Science*, Vol. 312, No. 5781, 1780-1782
- Peng, L.; Ran, L.; Chen, H.; Zhang, H.; Kong, J. A. & Grzegorzczak, T. M. (2007). Experimental observation of left-handed behavior in an array of standard dielectric resonators. *Phys. Rev. Lett.*, Vol. 98, No. 15, 157403
- Pozar, D. M. (2004). *Microwave Engineering*, Wiley, New York.
- Rachford, F. J.; Armstead, D. N.; Harris, V. G. & Vittoria, C. (2007). Simulations of ferrite-dielectric-wire composite negative index materials. *Phys. Rev. Lett.*, Vol. 99, No. 05, 057202
- Rikken, G. L. J. A. & van Tiggelen, B. A. (1996). Observation of magnetically induced transverse diffusion of light. *Nature*, Vol. 381, No. 6577, 54-55
- Sarychev, A. K.; McPhedran, R. C. & Shalaev, V. M. (2000). Electrodynamics of metal-dielectric composites and electromagnetic crystals. *Phys. Rev. B*, Vol. 62, No. 12, 8531-8539
- Schurig, D.; Mock, J. J.; Justice, B. J.; Cummer, S. A.; Pendry, J. B.; Starr, A. F. & Smith, D. R. (2006). Metamaterial electromagnetic cloak at microwave frequencies. *Science*, Vol. 314, No. 5801, 977-980
- Shalaev, V. M. (2007). Optical negative-index metamaterials. *Nature Photon.*, Vol. 1, No. 1, 41-48
- Shelby, R. A.; Smith, D. R. & Schultz S. (2001). Experimental verification of a negative index of reflection. *Science*, Vol. 292, No. 5514, 77-79
- Sheng, P. (1995). *Introduction to Wave Scattering, Localization, and Mesoscopic Phenomena*, Academic Press, San Diego.
- Sigalas, M. M.; Soukoulis, C. M.; Biswas, R. & Ho, K. M. (1997). Effect of the magnetic permeability on photonic band gaps. *Phys. Rev. B*, Vol. 56, No. 3, 959-962
- Silveirinha, M. & Engheta, N. (2006). Tunneling of electromagnetic energy through subwavelength channels and bends using ϵ -near-zero materials. *Phys. Rev. Lett.*, Vol. 97, No. 15, 157403
- Smith, D. R.; Schultz, S.; Markoš, P. & Soukoulis, C. M. (2002). Determination of effective permittivity and permeability of metamaterials from reflection and transmission coefficients. *Phys. Rev. B*, Vol. 65, No. 19, 195104
- Smith, D. R.; Vier, D. C.; Koschny, T. & Soukoulis, C. M. (2005). Electromagnetic parameter retrieval from inhomogeneous metamaterials. *Phys. Rev. E*, Vol. 71, No. 3, 036617
- Stefanou, N.; Yannopapas, V. & Modinos, A. (1998). Heterostructures of photonic crystals:

- frequency bands and transmission coefficients. *Compu. Phys. Commun.*, Vol. 113, No. 1, 49-77
- Valentine, J.; Zhang, S.; Zentgraf, T.; Ulin-Avila, E.; Genov, D. A.; Bartal, G. & Zhang, X. (2008). Three-dimensional optical metamaterial with a negative refractive index. *Nature*, Vol. 455, No. 7211, 376-379
- Veselago, V. C. (1968). The electrodynamics of substrates with simultaneously negative values of ϵ and μ . *Sov. Phys. Usp.*, Vol. 10, No. 4, 509-514
- Wang, Z.; Chong, Y. D.; Joannopoulos, J. D. & Soljačić, M. (2008). Reflection-free one-way edge modes in a gyromagnetic photonic crystal. *Phys. Rev. Lett.*, Vol. 100, No. 1, 013905
- Wang, Z.; Chong, Y. D.; Joannopoulos, J. D. & Soljačić, M. (2009). Observation of unidirectional backscattering-immune topological electromagnetic states. *Nature*, Vol. 461, No. 7265, 772-775
- Wu, Y.; Li, J.; Zhang, Z. Q. & Chan, C. T. (2006). Effective medium theory for magnetodielectric composites: Beyond the long-wavelength limit. *Phys. Rev. B*, Vol. 74, No. 8, 085111
- Wu, Y.; Lai, Y. & Zhang, Z. Q. (2007). Effective medium theory for elastic metamaterials in two dimensions. *Phys. Rev. B*, Vol. 76, No. 20, 205313
- Xu, C.; Han, D.; Wang, X.; Liu, X. & Zi, J. (2007). Extrinsic photonic crystals: Photonic band structure calculations of a doped semiconductor under a magnetic field. *Appl. Phys. Lett.*, Vol. 90, No. 6, 061112
- Yablonovitch, E. (1987). Inhibited spontaneous emission in solid state physics and electronics. *Phys. Rev. Lett.*, Vol. 58, No. 20, 2059-2062
- Yannopapas, V. & Vitinov, N. V. (2006). Photoexcitation-induced magnetism in arrays of semiconductor nanoparticles with a strong excitonic oscillator strength. *Phys. Rev. B*, Vol. 74, No. 19, 193304
- Yu, Z. F.; Veronis, G.; Wang, Z. & Fan, S. H. (2008). One-Way electromagnetic waveguide formed at the interface between a plasmonic metal under a static magnetic field and a photonic crystal. *Phys. Rev. Lett.*, Vol 100, No. 2, 023902
- Zhang, S.; Fan, W.; Panoiu, N. C.; Malloy, K. J.; Osgood, R. M. & Brueck, S. R. J. (2005). Experimental demonstration of near-infrared negative-index metamaterials. *Phys. Rev. Lett.*, Vol. 95, No. 13, 137404
- Zhang, S.; Park, Y. S.; Li, J.; Lu, X.; Zhang, W. & Zhang, X. (2009). Negative refractive index in chiral metamaterials. *Phys. Rev. Lett.*, Vol. 102, No. 2, 023901
- Zayats, A. V.; Smolyaninov, I. I. & Maradudin, A. A. (2005). Nano-optics of surface plasmon polaritons. *Phys. Rep.*, Vol. 408, No. 3-4, 131-314



Wave Propagation

Edited by Dr. Andrey Petrin

ISBN 978-953-307-275-3

Hard cover, 570 pages

Publisher InTech

Published online 16, March, 2011

Published in print edition March, 2011

The book collects original and innovative research studies of the experienced and actively working scientists in the field of wave propagation which produced new methods in this area of research and obtained new and important results. Every chapter of this book is the result of the authors achieved in the particular field of research. The themes of the studies vary from investigation on modern applications such as metamaterials, photonic crystals and nanofocusing of light to the traditional engineering applications of electrodynamics such as antennas, waveguides and radar investigations.

How to reference

In order to correctly reference this scholarly work, feel free to copy and paste the following:

Shiyang Liu, Zhifang Lin and S. T. Chui (2011). Manipulating the Electromagnetic Wave with a Magnetic Field, Wave Propagation, Dr. Andrey Petrin (Ed.), ISBN: 978-953-307-275-3, InTech, Available from:
<http://www.intechopen.com/books/wave-propagation/manipulating-the-electromagnetic-wave-with-a-magnetic-field>

INTECH
open science | open minds

InTech Europe

University Campus STeP Ri
Slavka Krautzeka 83/A
51000 Rijeka, Croatia
Phone: +385 (51) 770 447
Fax: +385 (51) 686 166
www.intechopen.com

InTech China

Unit 405, Office Block, Hotel Equatorial Shanghai
No.65, Yan An Road (West), Shanghai, 200040, China
中国上海市延安西路65号上海国际贵都大饭店办公楼405单元
Phone: +86-21-62489820
Fax: +86-21-62489821

© 2011 The Author(s). Licensee IntechOpen. This chapter is distributed under the terms of the [Creative Commons Attribution-NonCommercial-ShareAlike-3.0 License](#), which permits use, distribution and reproduction for non-commercial purposes, provided the original is properly cited and derivative works building on this content are distributed under the same license.

IntechOpen

IntechOpen